





Multifunctional piezoelectric hydrogels under ultrasound stimulation boost chondrogenesis by recruiting autologous stem cells and activating the Ca^{2+} /CaM/CaN signaling pathway

Yu-Bao Liu^{a,1}, Xu Liu^{b,f,1}, Xiao-Fei Li^{a,1}, Liang Qiao^{c,1}, Hao-Liang Wang^a, Yue-Fu Dong^d, Feng Zhang^e, Yang Liu^g, Hao-Yang Liu^a, Ming-Liang Ji^a, Lan Li^{c,h,***}, Qing Jiang^{c,h,**}, Jun Lu^{a,*}

^a The Center of Joint and Sports Medicine, Orthopedics Department, Zhongda Hospital, School of Medicine, Southeast University, Nanjing, 210009, China

^b Department of Orthopedics, The Yangzhou Clinical Medical College of Xuzhou Medical University, Yangzhou, 225009, China

^c Division of Sports Medicine and Adult Reconstructive Surgery, Department of Orthopedic Surgery, Nanjing Drum Tower Hospital, Affiliated Hospital of Medical School, Nanjing University, Nanjing, 210008, China

^d Department of Joint Surgery, The First People's Hospital of Lianyungang City, Lianyungang, 222000, China

^e Orthopedics Department, Xuyi County People's Hospital, Huai'an, 211700, China

^f Orthopedics Department, Nanjing Drum Tower Hospital & Group's Suqian Hospital, Affiliated Hospital of Medical School, Nanjing University, Suqian, 223800, China

^g Orthopedics Department, Dan Yang Third People's Hospital, Zhenjiang, 212300, China

^h Institute of Medical 3D Printing, Nanjing University, Nanjing, 210093, China

ARTICLE INFO

Keywords:

Piezoelectric hydrogel
Ultrasound stimulation
Bioadhesiveness
Chondrogenesis
Calcium ion

ABSTRACT

Articular cartilage, owing to the lack of undifferentiated stem cells after injury, faces significant challenges in reconstruction and repair, making it a major clinical challenge. Therefore, there is an urgent need to design a multifunctional hydrogels capable of recruiting autologous stem cells to achieve *in situ* cartilage regeneration. Here, our study investigated the potential of a piezoelectric hydrogel (Hyd₆) for enhancing cartilage regeneration through ultrasound (US) stimulation. Hyd₆ has multiple properties including injectability, self-healing capabilities, and piezoelectric characteristics. These properties synergistically promote stem cell chondrogenesis. The fabrication and characterization of Hyd₆ revealed its excellent biocompatibility, biodegradability, and electro-mechanical conversion capabilities. *In vitro* and *in vivo* experiments revealed that Hyd₆, when combined with US stimulation, significantly promotes the recruitment of autologous stem cells and enhances chondrogenesis by generating electrical signals that promote the influx of Ca^{2+} , activating downstream CaM/CaN signaling pathways and accelerating cartilage formation. An *in vivo* study in a rabbit model of chondral defects revealed that Hyd₆ combined with US treatment significantly improved cartilage regeneration, as evidenced by better integration of the regenerated tissue with the surrounding cartilage, greater collagen type II expression, and improved mechanical properties. The results highlight the potential of Hyd₆ as a novel therapeutic approach for treating cartilage injuries, offering a self-powered, noninvasive, and effective strategy for tissue engineering and regenerative medicine.

Peer review under the responsibility of editorial board of Bioactive Materials.

* Corresponding author.

** Corresponding author. Division of Sports Medicine and Adult Reconstructive Surgery, Department of Orthopedic Surgery, Nanjing Drum Tower Hospital, Affiliated Hospital of Medical School, Nanjing University, Nanjing, 210008, China.

*** Corresponding author. Division of Sports Medicine and Adult Reconstructive Surgery, Department of Orthopedic Surgery, Nanjing Drum Tower Hospital, Affiliated Hospital of Medical School, Nanjing University, Nanjing, 210008, China.

E-mail addresses: lanl17@163.com (L. Li), qingj@nju.edu.cn (Q. Jiang), lujun-joint@seu.edu.cn (J. Lu).

¹ Yu-Bao Liu, Xu Liu, Xiao-Fei Li and Liang Qiao contributed equally to this paper.

<https://doi.org/10.1016/j.bioactmat.2025.04.009>

Received 20 January 2025; Received in revised form 25 March 2025; Accepted 10 April 2025

2452-199X/© 2025 The Authors. Publishing services by Elsevier B.V. on behalf of KeAi Communications Co. Ltd. This is an open access article under the CC BY-NC-ND license (<http://creativecommons.org/licenses/by-nc-nd/4.0/>).

1. Introduction

Cartilage injuries are prevalent clinical issues that affect millions of individuals worldwide and lead to significant morbidity and impaired quality of life [1]. The incidence of cartilage damage is particularly high in athletes and elderly individuals, with conditions such as osteoarthritis contributing to the deterioration of cartilage tissue [2]. Unfortunately, cartilage has a limited capacity for self-repair because of its avascular nature and low cellularity, often resulting in chronic pain and disability [3]. Current treatment options, including surgical interventions and pharmacological therapies, frequently fall short of providing long-term relief or restoring the functional integrity of the cartilage [4]. Moreover, existing strategies often fail to address the underlying biological mechanisms involved in cartilage regeneration, leading to suboptimal outcomes [5]. As a result, there is an urgent need for innovative therapeutic approaches that can effectively enhance cartilage repair and regeneration. Recent advancements in biomaterials have shown promise; however, the integration of novel properties, such as piezoelectricity and ultrasound (US) stimulation, remains underexplored. This gap highlights the necessity for further research to develop effective strategies for cartilage regeneration that can overcome the limitations of current clinical practices.

Piezocatalytic therapy (PT) is a treatment method that uses the electric fields or charges generated by piezoelectric materials under mechanical stress to promote biomedical applications, showing great potential in the fields of tissue engineering and regenerative medicine [6]. Piezoelectric materials can accumulate charges and exhibit electrical activity when subjected to external mechanical stresses (such as breathing, heartbeat, blood flow, and slight body movements), and these electrical activities can be harnessed to promote tissue regeneration and repair [7]. For example, piezoelectric materials enhance cellular responses under stress-driven conditions, particularly their role in promoting stem cell chondrogenic differentiation through mechanical and electrical cues [8]. Piezoelectric hydrogels made from short electrospun poly-L-lactic acid nanofibers embedded in a collagen matrix can be injected into joints and self-generate local electrical cues under US activation to drive cartilage healing [9]. This self-powered treatment method provides new strategies for regenerative medicine, offering advantages over traditional tissue engineering “three elements,” [10] such as the absence of any biological inductive factors, no need for exogenous seed cells, noninvasiveness, and good biocompatibility [11]. During the piezoelectric catalytic therapy process, the piezoelectric potential activates voltage-gated calcium channels (VGCC), facilitating the influx of calcium ions into cells, thereby activating various signaling pathways and accelerating cartilage formation [12]. Sodium potassium niobate (KNN) is a lead-free piezoelectric ceramic that can convert mechanical energy into electrical energy through the positive piezoelectric effect, activating many intracellular signaling pathways that influence cell migration, proliferation, and differentiation [13]. These findings suggest that KNN nanoparticles can generate local electrical cues through US irradiation to drive cartilage healing.

In addition to efficient piezoelectric catalytic capabilities, a harmonious microenvironment is crucial for the regeneration of complex defects. Owing due to their ability to provide an ordered three-dimensional network structure, tunable mechanical properties, and excellent biocompatibility, hydrogels have attracted widespread attention in biomedical engineering [14]. In recent years, significant advancements have been made in the application of hydrogels for cartilage repair. Hydrogels can effectively mimic the extracellular matrix (ECM) of cartilage and offer substantial potential for constructing cartilage organoids (CORGs) that replicate the structure and function of native cartilage [15]. Among these materials, silk fibroin hydrogels, with their EC-like structure, unique mechanical properties, and excellent biocompatibility, have emerged as ideal materials for building CORGs. These hydrogels can be fabricated through various cross-linking methods, including enzymatic cross-linking, photopolymerization, and physical

cross-linking, to precisely control their properties. Moreover, after functional modification with synthetic and natural materials, they have shown significantly improved mechanical strength, water retention, antibacterial properties, and cartilage repair capabilities [16]. DNA hydrogels have the capacity to precisely control stress relaxation, cross-linking thermodynamics, kinetics, and degradability, making them highly adaptable for tissue engineering applications. By combining DNA hydrogels with other materials (such as polylysine or silk fibroin), hybrid hydrogels with enhanced mechanical properties and resistance to enzymatic degradation have been developed, further enhancing their potential for cartilage repair [17]. Additionally, DNA hydrogels loaded with extracellular vesicles (EVs) can form a three-dimensional network that supports cell adhesion and proliferation, thereby enhancing cartilage regeneration through the promotion of cell proliferation and differentiation [18]. However, the variable shapes and depths of defects make it difficult for general hydrogels to effectively cover complex defects [19]. Therefore, injectable hydrogels with adaptive functions that can automatically change shape to match the defect site have become ideal filling dressings [20]. Unfortunately, most injectable hydrogels have poor mechanical toughness and are prone to damage or fracture under repeated external forces [21]. Thus, injectable hydrogels with rapid self-healing capabilities are crucial for restoring the stability of the preinjury scaffold structure. Additionally, hydrogel scaffolds should also possess the ability to withstand significant mechanical cyclic loads to accommodate the long-term burden of joint movement [22]. Recent studies have demonstrated that hydrogels with high mechanical performance have significant clinical advantages in joint cartilage regeneration [14]. Concurrently, the adherence and prolonged retention of multifunctional biomaterials at the defect location are essential elements in cartilage regeneration. However, achieving strong wet tissue adhesion in various fluid environments, including synovial fluid, poses a significant challenge for hydrogel adhesion. Inspired by the catechol functional groups found in marine mussels, which are key structures for strong wet adhesion, hydrogels containing catechol groups have received widespread attention [23]. However, catechol groups can easily oxidize to quinones in the presence of oxygen in the air, which may affect the material's adhesion properties and biocompatibility [24]. To overcome this difficulty, we developed a novel adhesive hydrogel with high hydrogen bond density. Polyvinyl alcohol (PVA), Owing to its small hydroxyl volume, PVA, which can form strong hydrogen bonds between molecules, along with the physical entanglement between PVA chains, was selected as the main component of the strong bioadhesive hydrogel dressing [25]. Polyacrylic acid (PAA) contains a rich and uniformly distributed carboxyl functional group in its molecular chain, which can dynamically cross-link with hydrogen bonds between PVA molecules, forming a dual interpenetrating network hydrogel that provides strong adhesion for wet tissues [26,27]. Additionally, injectable chitosan (CS)-based hydrogels can form gels *in situ* through rapid interpenetration and entanglement according to body temperature changes, tightly filling various irregular wound surfaces [28] and showing promising translational potential in tissue engineering. The dynamic hydrogen bond cross-linking and covalent cross-linking between CS, PVA, and PAA, along with physical entanglement, endow the hydrogel with rapid autonomous healing capabilities, strong and durable adhesion, and excellent mechanical properties.

This study aims to explore the innovative potential of the piezoelectric hydrogel PVA/PAA/CS/KNN (KNN-Hyd) in enhancing cartilage regeneration through US stimulation (Fig. 1). The primary objective of this study was to investigate the multifunctional properties of KNN-Hyd, particularly its injectability, self-healing capabilities, and piezoelectric characteristics, and how these properties can synergistically promote the chondrogenic differentiation of stem cells. By integrating US stimulation with the unique attributes of KNN-Hyd, this research sought to elucidate the underlying mechanisms that govern cellular responses and tissue repair processes. The significance of this research lies in its potential to bridge the existing knowledge gap in cartilage repair

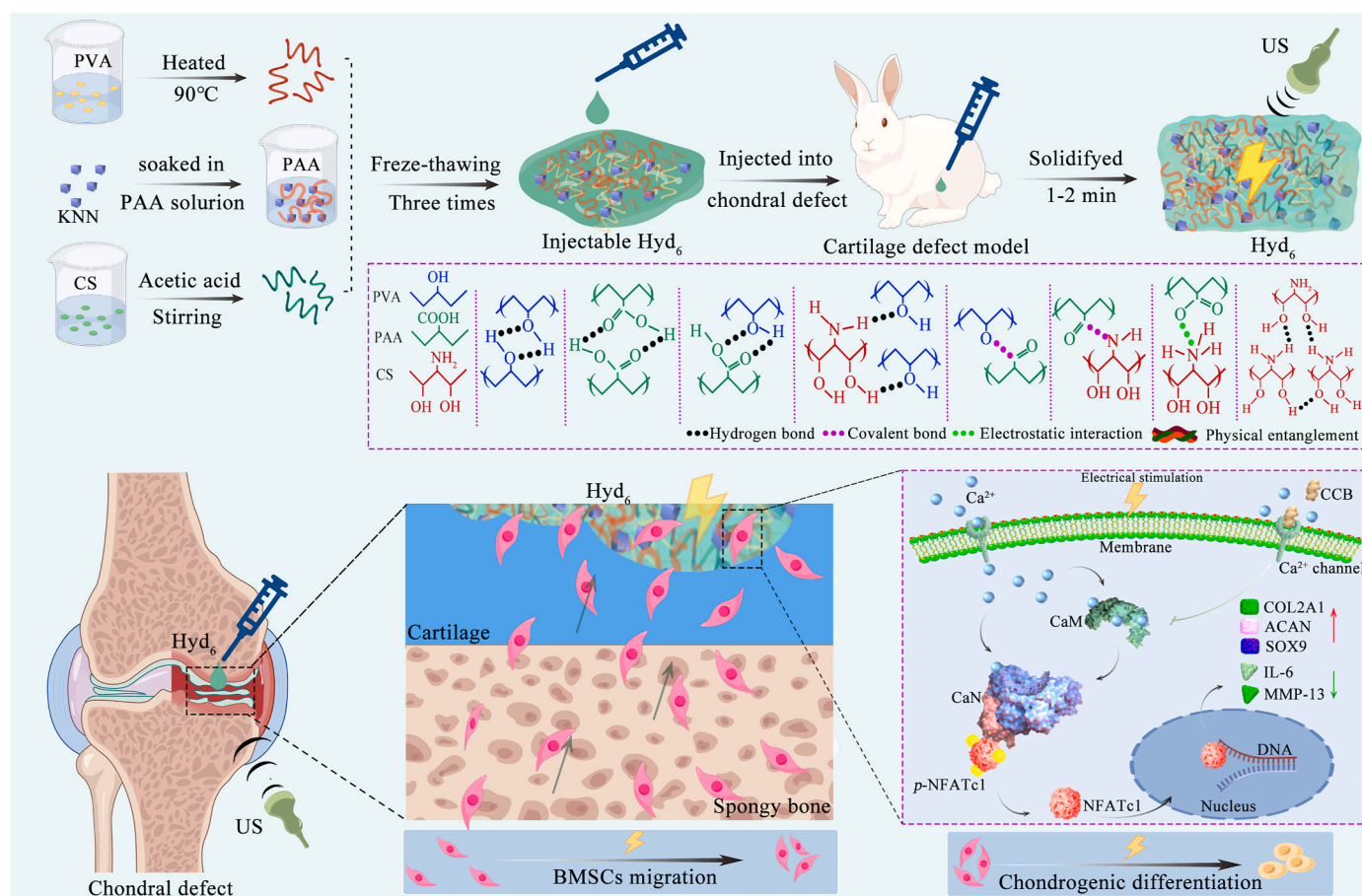


Fig. 1. Schematic illustration of PVA/PAA/CS/KNN hydrogel preparation and its synergistic effect with US-driven piezoelectric stimulation therapy in repairing cartilage defects (by Figdraw).

strategies, offering a novel therapeutic approach that combines biomaterials with advanced stimulation techniques. These findings could pave the way for the development of more effective treatments for cartilage injuries, ultimately improving patient outcomes and quality of life. Furthermore, this study contributes to the broader field of regenerative medicine by providing insights into the interactions between piezoelectric materials and biological systems, thereby fostering future innovations in tissue engineering and repair methodologies.

2. Results and discussion

2.1. Fabrication and characterization of the KNN-Hyd piezoelectric hydrogel

Piezoelectric hydrogels have significant application potential in biosensing, cellular fate determination, and tissue regeneration owing to their remarkable biocompatibility, exceptional biodegradability, and effective electromechanical conversion [29]. We first synthesized a KNN-Hyd injectable piezoelectric hydrogel by combining physical mixing with chemical crosslinking through H-bonding, electrostatic interactions and physical entanglement (Fig. 2a), and the resulting scaffold could be constructed with varying weight percentages of KNN (Table S1). The transmission electron microscopy (TEM) images reveal that the KNN nanoparticles have an irregular cubic shape (Fig. 2b). The measurement results revealed that the mean diameter of the KNN nanoparticles was 21.8 ± 7.4 nm (Fig. S1a). Scanning electron microscopy (SEM) was used to observe the morphology of KNN-Hyd, and the images revealed that the scaffold features an irregular porous structure and an internal framework, with numerous KNN nanoparticles

incorporated into the interconnected pore walls of the hydrogel (Fig. S1b). Fig. S1c shows the SEM image coupled with element mapping for Nb, Na, K, C, N, and O in a KNN-Hyd sample. After the hydrogel was freeze-dried, the scaffolds exhibited a porous configuration (Fig. 2c), and the mean pore sizes of Hyd₃, Hyd₆, and Hyd₉ (the mass fractions of the KNN nanoparticles in KNN-Hyd were 3 wt%, 6 wt%, and 9 wt% respectively) were 14, 10, and 18 μm , respectively (Fig. 2d). The variation in pore sizes could be attributed to the increased crosslinking density within the network structure.

The XRD patterns of the piezoelectric hydrogels revealed that the diffraction peaks associated with KNN nanoparticles were (100), (110), (111), (200), (210), and (022), indicating that the KNN nanoparticles possess a cubic perovskite structure and demonstrating the piezoelectric properties of the KNN nanoparticles (Fig. 2e). The hydrogels were examined via Fourier transform infrared (FTIR) spectroscopy to explore their chemical composition (Fig. 2f). The FTIR spectra of PVA, PAA, and CS were somewhat similar, especially at 3439 cm^{-1} (-OH bending vibration and N-H stretching vibration in -NH₂), 2929 cm^{-1} (C-H stretching vibration), 1732 cm^{-1} (C=O stretching vibration in the ester group), 1451 cm^{-1} (C-N stretching vibration), 842 cm^{-1} , and 661 cm^{-1} (C-O stretching vibration in COOH). All the composite scaffold spectra presented characteristic absorption peaks for KNN-Hyd, confirming that each KNN-Hyd scaffold contained a blend of parental materials.

The microstructure of hydrogels is the basis of their mechanical behavior [30]. The rheological characteristics of the KNN-Hyd were examined via a rheometer, and the changes in the storage modulus (G') and loss modulus (G'') of the scaffolds over time were recorded. KNN-Hyd had a stable modulus (Fig. 2g). As the KNN nanoparticle content increased, the G' value initially increased but then decreased,

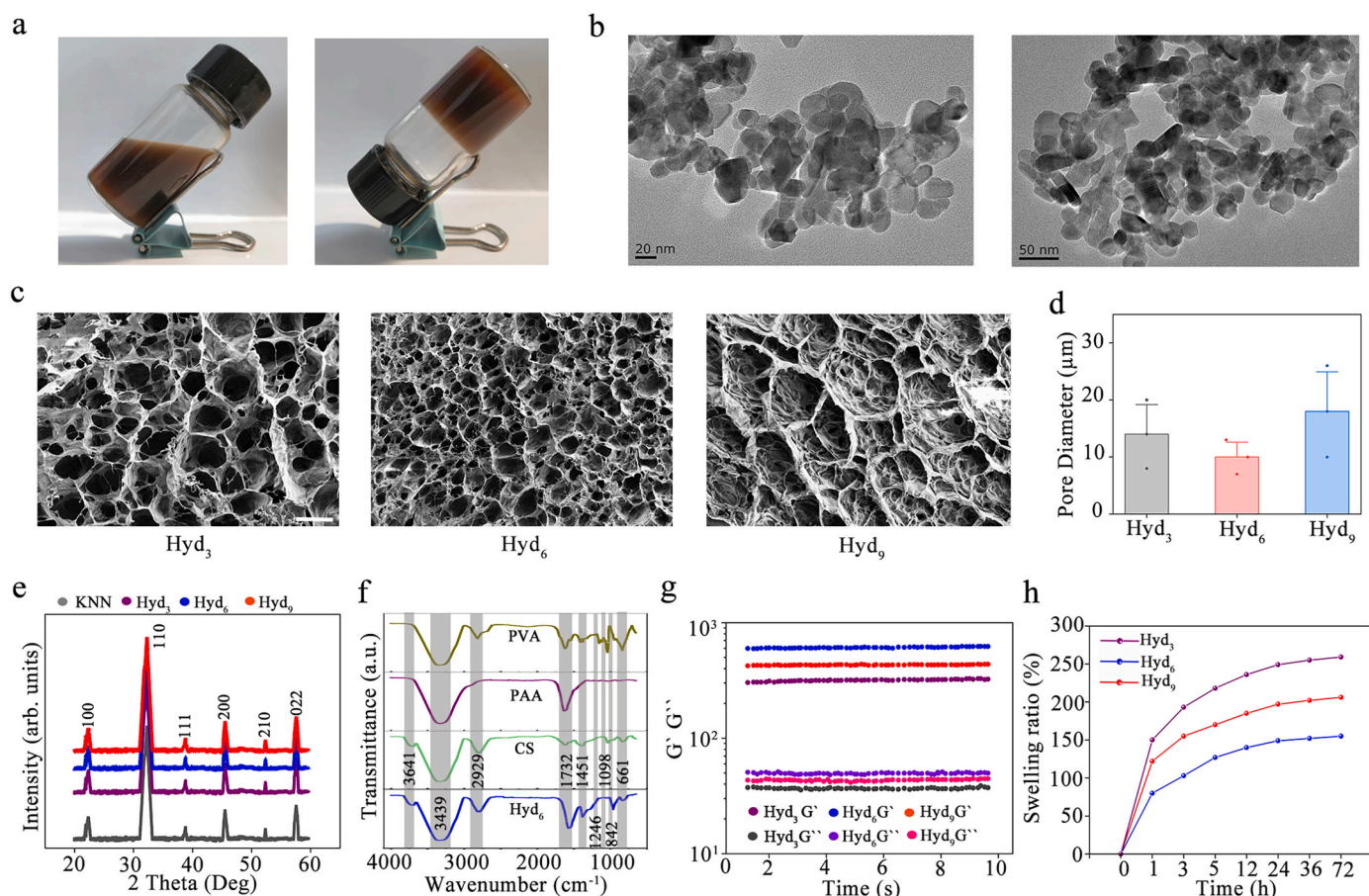


Fig. 2. Characterization of the prepared KNN-Hyd. (a) Photographs of liquid KNN-Hyd and solidified KNN-Hyd. (b) TEM image of the KNN nanoparticles. (c) SEM images of hydrogels with different contents of KNN. Scale bars: 20 μm. (d) Pore diameter of the hydrogels. (e) XRD patterns of KNN-Hyd. (f) FTIR spectra of the hydrogels. (g) Rheological behavior of the hydrogels. (h) Swelling ratios of hydrogels.

indicating that multiple H-bonds, electrostatic interactions, and physical entanglement could augment the mechanical properties of the scaffold. However, an excessively high content of KNN might reduce the mechanical properties.

As a suitable filling agent for fixed-size defects, the adhesive hydrogel should not expand excessively upon absorbing bodily fluids, which facilitates the healing of the defect [31]. Consequently, the swelling abilities of the aforementioned hydrogels were assessed in phosphate-buffered saline (PBS) at 37 °C. As illustrated in Fig. 2h, the swelling rates of the hydrogels steadily increased with increasing incubation time, attaining equilibrium swelling conditions after approximately 5 h. The swelling ratio of Hyd₆ was 120 %, which was significantly lower than those of Hyd₃ and Hyd₉. This might be because Hyd₆ possesses the optimal cross-linking network density, which aligns with the hydrogel pore dimension and storage modulus findings. Nevertheless, we believe that the swelling rate of Hyd₆ remains sufficiently stable to effectively fill defects.

2.2. Assays of the multifunctional properties of KNN-Hyd

2.2.1. Injectability and gelation

In situ formed injectable hydrogels have promising applications because of their ability to automatically seal complex and irregular shapes [32]. A rheometer was used to perform rotational tests on the hydrogels to observe whether they exhibited shear thinning behavior after transitioning into a fluid state. The viscosity of Hyd₆ increased as the shear rate increased (Fig. 3a), confirming the shear-thinning behavior of the scaffold. We filled Hyd₆ into a syringe needle and ultimately extruded the hydrogel (inset of Fig. 3a), demonstrating the

injectability of KNN-Hyd.

To determine the gelation time of KNN-Hyd, we ran strain sweep tests. On the basis of the time sweep test, Hyd₆ underwent rapid solidification at 1 Hz and achieved a structure with a modulus of approximately 80 Pa in approximately 2 min (Fig. 3b). As shown in the inset of Fig. 3b, the solidified Hyd₆ established a stable configuration at 37 °C within 2 min.

2.2.2. Self-healing behavior

After solidifying at the defect site, the hydrogel may undergo high-frequency movements and be subjected to repeated external mechanical compression. Therefore, self-healing hydrogels extend the lifespan of a material not only by restoring its predamaged shape but also by restoring its predamaged performance [33]. To evaluate the self-healing characteristics of the hydrogel, rheological recovery tests were performed on Hyd₆ at an angular frequency of 10 rad/s. The findings from the strain amplitude sweep test indicated that when the stress was increased to $\gamma = 400$ %, the G' and G'' curves of Hyd₆ decreased steeply, and $G'' > G'$, indicating the threshold of disintegration of the hydrogel network (Fig. 3c). After the stress was restored to its initial state, G' and G'' promptly reverted to their initial values. After multiple cycles, G' did not significantly decrease (Fig. 3d), illustrating the self-healing capability of Hyd₆. This self-healing effect of the hydrogel could be attributed to the dynamic reactions among diverse dynamic functional groups within the piezoelectric scaffold.

2.2.3. Adhesive capacity

To ensure that the hydrogel does not detach during movement when it is filled with different materials, the scaffold should also possess

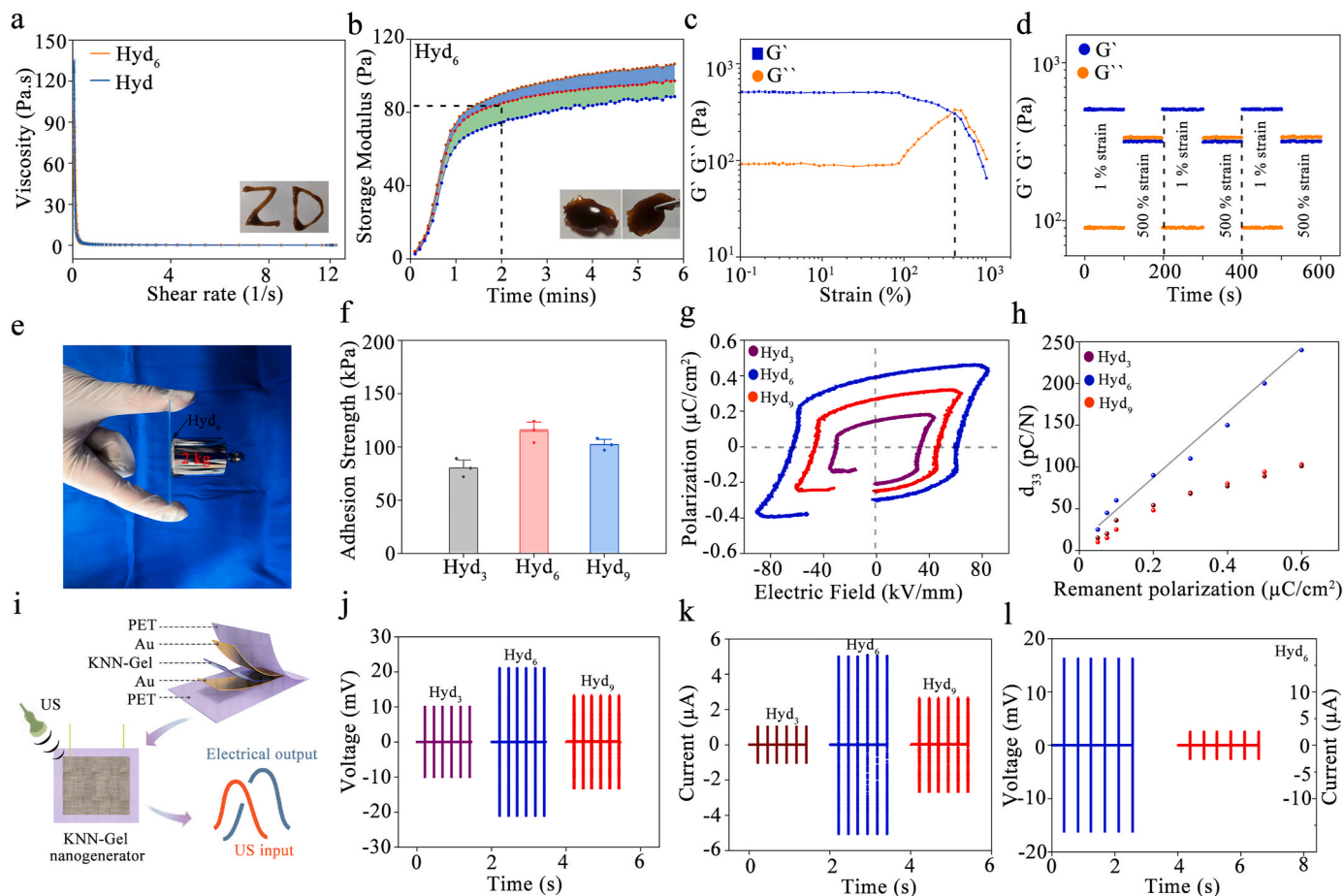


Fig. 3. Injectable, self-healing, adhesive and piezoelectric properties of the KNN-Hyd and electrical characterization of the nanogenerators made of Hyd₆. (a) Viscosity measurement of Hyd₆ and Hyd hydrogels. (Inset: Display of injectability of the hydrogel). (b) Time sweep testing to determine the gelation time of Hyd₆ at 37 °C. (Inset: Display of solidification of the hydrogel). (c) Strain amplitude sweep test of self-healing Hyd₆ with strains ranging from 1 % to 1000 % (1 Hz). (d) Amplitude oscillation strain test of Hyd₆ with alternating strains ranging from 1 % to 700 % for three cycles. (e) Photograph of the lap-shear test. (f) Adhesive strength of hydrogels with different contents of KNN between different substances. (g) Polarization hysteresis loops of hydrogels with different contents of KNN under the same poling electric fields. (h) Piezoelectric coefficient (d_{33}) of hydrogels with different contents of KNN as a function of the remanent polarization. (i) Schematic illustration of the electrical output of nanogenerators made of KNN-Hyd under US excitation. (j) Open-circuit voltage generated by the nanogenerator made of KNN-Hyd under US excitation (US frequency of 40 kHz, pulse width of 5 μ s, pulse interval of 10 ms, and acoustic pressure of 100 kPa). (k) Short-circuit current generated by the nanogenerator made of KNN-Hyd under US excitation (US frequency of 40 kHz, pulse width of 5 μ s, pulse interval of 10 ms, and acoustic pressure of 100 kPa). (l) US response of nanogenerators made of Hyd₆ after implantation into a rabbit knee (US frequency of 40 kHz, pulse width of 5 μ s, pulse interval of 10 ms, and acoustic pressure of 100 kPa).

excellent adhesive strength. A lap shear test was performed using metal weights and glass slides to assess the adhesive characteristics of KNN-Hyd (Fig. 3e). As illustrated in Fig. 3f, all the scaffolds exhibited good bioadhesion properties, with Hyd₆ having the strongest adhesion force, reaching 110 kPa. The adhesive strength of the hydrogel to the substrate depends on the interfacial adhesion and cohesion of the hydrogel [34]. Carboxylic, hydroxyl, and amino groups rich in PVA, PAA, and CS increase the cross-linking density and enhance the cohesion of the hydrogel, whereas hydrogen bonds in the composite hydrogel improve the interfacial adhesion of the hydrogel. The adhesion strength of the hydrogel decreases with increasing KNN content, possibly due to a reduction in hydrogen bonding.

Frequent and complex movements of the joints, such as rotation, compression, and friction, might lead to delamination of the filled KNN-Hyd from the site of the defect. Therefore, we disrupted the Hyd₆ between the bonded weights and glass slides, reassembled the fractured hydrogel, and evaluated its adhesive properties after 30 min of healing. The results indicate that Hyd₆ possesses excellent self-healing properties and that the adhesive strength of the hydrogel following self-repair is slightly lower than its original adhesive strength (Fig. S2a), suggesting

that Hyd₆ could enable the reopening of the defect to close a second time.

2.2.4. Piezoelectric properties

The piezoelectric effect is the core of the biological effects produced by piezoelectric materials [35]. The most significant characteristic of piezoelectric ceramics is their ferroelectric properties [36]. Initially, the ferroelectricity of KNN-Hyd was measured via a ferroelectric testing system. As shown in Fig. 3g, a noticeable hysteresis curve was observed, suggesting the presence of a net dipole. Hyd₆ exhibited the largest P-E hysteresis. Theoretically, a higher content of KNN might result in stronger ferroelectricity, and the PE loop becomes more pronounced. However, when the KNN content reached 9 wt%, the PE loop diminished, probably due to the leakage conduction phenomenon of Hyd₉. The piezoelectric constant is a parameter that measures the ability of piezoelectric materials to transform mechanical energy into electrical energy [37]. The piezoelectric constant d_{33} of the KNN-Hyd piezoelectric support was subsequently tested. As depicted in Fig. 3h, the d_{33} value increases as the remanent polarization increases, and compared with the other two groups of hydrogels, Hyd₆ has the largest d_{33} .

Furthermore, a typical butterfly shaped amplitude loop was directly observed via piezoresponse force microscopy (PFM) (Fig. S2b), which confirmed that Hyd₆ has an excellent piezoelectric response. This indicates the presence of 180° domain walls and distinct polarization response switching behavior in Hyd₆, suggesting that it has good piezoelectric catalytic activity. Considering the various advantages of Hyd₆, we chose Hyd₆ as a representative to verify the diverse biological characteristics of the multifunctional hydrogel.

2.2.5. Electrical signal generation ability of the nanogenerators made of KNN-Hyd with US irradiation in vitro and in vivo

To measure the electrical output of the piezoelectric scaffold under US stimulation, we constructed a nanogenerator made of KNN-Hyd (Fig. 3i). The US irradiation parameters were as follows: 40 kHz [9], 100 kPa, pulse duration: 5 μ s, and pulse spacing: 10 ms [38]. Under an acoustic pressure of 100 kPa, the voltages of the nanofiber nanogenerators made of Hyd₃, Hyd₆, and Hyd₉ were 9.9 mV, 21.0 mV, and 13.2 mV, respectively (Fig. 3j), and the currents of the nanofiber nanogenerators made of Hyd₃, Hyd₆, and Hyd₉ were 1.0 μ A, 5.0 μ A, and

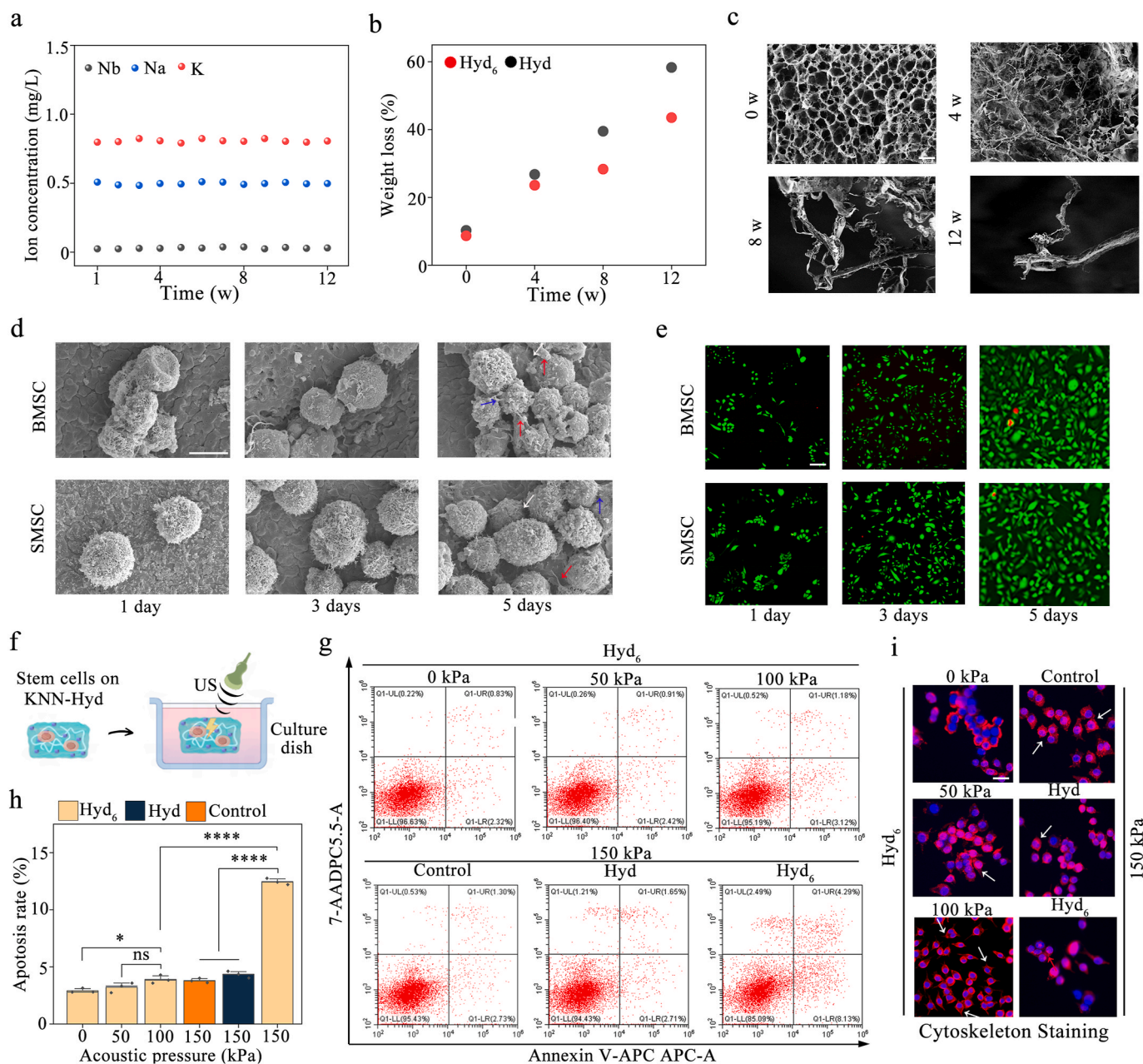


Fig. 4. Biodegradable behavior and biocompatibility of KNN-Hyd and ultrasonic tolerance analysis. (a) Ion concentrations detected in the saline solution after soaking with KNN nanoparticles for different durations. (b) Time-dependent weight loss of KNN-Hyd soaked in PBS (pH 7.4, 37 °C). (c) SEM images of Hyd₆ soaked in PBS (pH 7.4, 37 °C) for different durations (0, 4, 8, and 12 weeks). Scale bars: 20 μ m. (d) SEM images of the BMSCs and SMSCs seeded on Hyd₆ after 1, 3, and 5 days. Red arrows indicate filopodia. The blue arrows indicate cell adhesion. The white arrows indicate cell adhesion to the hydrogel. Scale bars: 5 μ m. (e) Live/dead cell staining of the BMSCs and SMSCs cocultured with Hyd₆ after 1, 3, and 5 days. Scale bars: 100 μ m (f) Schematic diagram of the BMSCs seeded on the KNN-Hyd scaffolds combined with US (by Figdraw). (g) Effect of US treatment on BMSC apoptosis on different hydrogels after 5 days. (h) Statistical analysis of the effects of US treatment on BMSC apoptosis on different hydrogels after 5 days. (i) Confocal microscopy images of the cytoskeleton of BMSCs cultured on different hydrogels after 5 days of US treatment. Red = Phalloidin and actin staining. Blue = DAPI, nucleus staining. The white arrows indicate filopodia. Scale bars: 20 μ m ns $p > 0.05$, * $p < 0.05$, and **** $p < 0.0001$.

2.6 μA , respectively (Fig. 3k). The electrical output of Hyd₆ is the highest, followed by that of Hyd₉, and that of Hyd₃ is the lowest; these results are consistent with the piezoelectric characteristics.

Considering the excellent electrical output performance of Hyd₆, we selected a nanogenerator made of Hyd₆ to explore the potential reduction in US intensity during *in vivo* stimulation. We inserted the nanogenerator into the cartilage defect site of a rabbit knee (Fig. S3a). Following implantation, the voltage and current of the US-powered nanogenerator were approximately 16.1 mV and 2.5 μA , respectively (Fig. 3l). Apparently, the output performance decreases due to the reduction in US intensity in biological tissues; however, this reduction is minimal in our experiments involving deep tissues of small animals.

Maintaining a stable piezoelectric output is a prerequisite for effective tissue repair mediated by piezoelectric hydrogels. To this end, we evaluated the potential effects of prolonged US stimulation on the piezoelectric capability of the hydrogel scaffolds. Hyd₆ cells were continuously immersed in saline at 37 °C and subjected to parametrized US stimulation (20 or 60 min per day) (Fig. S3b). The samples were then retrieved at predefined time points (2, 4, 6, and 8 weeks) and used to construct nanogenerators for quantitative assessment of their piezoelectric properties. Moreover, prolonged US irradiation accelerated the decrease in the d_{33} of the hydrogel scaffolds. Moreover, after extended US stimulation, the d_{33} of Hyd₆ was significantly reduced (Fig. S3c). These results indicate that the duration of US irradiation is negatively correlated with the piezoelectric properties of the hydrogels in a dose-dependent manner. When exposed to 20 min of US irradiation daily, Hyd₆ exhibited a gradual decline in voltage and current output over the experimental period. After 8 weeks, the voltage and current decreased by only 2 mV and 0.3 μA , respectively, indicating that short-term US irradiation, although causing some degradation in piezoelectric performance, still maintained stable electromechanical conversion capabilities. In contrast, when subjected to 60 min of daily US irradiation, the rate of electrical output decay in the piezoelectric hydrogels was significantly accelerated (Figs. S3d and e). These results demonstrate a pronounced time-dependent attenuation relationship between the duration of US irradiation and the output charge of the nanogenerator.

2.2.6. Biodegradability and biocompatibility

Biodegradability is an essential criterion for the utilization of hydrogels in the biomedical domain [39]. We independently introduced KNN nanoparticles and Hyd₆ hydrogels into a 37 °C PBS solution to examine their degradation performance. Initially, we employed a spectrometer to assess the degradation of KNN nanoparticles. The findings indicated that over the duration from 1 to 12 weeks, Na^+ , K^+ , and Nb^{5+} were continuously released. The levels of released Na^+ , K^+ , and Nb^{5+} were 0.8 mg/L, 0.5 mg/L, and 0.02 mg/L, respectively (Fig. 4a). These results imply the biodegradability of KNN. The mass loss progression of the Hyd₆ piezoelectric scaffold was subsequently evaluated over a 12-week period, with the PVA/PAA/CS hydrogel (Hyd) used as the control. The quality of Hyd and Hyd₆ markedly decreased with prolonged soaking in PBS (Fig. 4b). By the conclusion of the 12th week, the mass reductions of Hyd and Hyd₆ were approximately 60 % and 42 %, respectively. Moreover, as illustrated in Fig. 4c, the surface morphology of Hyd₆ evolved throughout the degradation timeline (0, 4, 8, and 12 weeks). Consequently, the Hyd₆ piezoelectric scaffold can ultimately undergo biodegradation.

Bone marrow mesenchymal stem cells (BMSCs) and synovial mesenchymal stem cells (SMSCs) are present *in situ* within the joint cavity [40]. When cartilage is damaged, “dormant” BMSCs are “awakened” and migrate to the site of injury, where they differentiate into chondrocytes [41]; moreover, SMSCs are also capable of migrating from synovial tissue to damaged cartilage to repair cartilage injury [42]. Therefore, we selected rabbit-derived BMSCs and mouse-derived SMSCs to assess the impact of Hyd₆ in conjunction with US on stem cell activity. SEM was used to observe the morphology of the stem cells seeded on the Hyd₆ scaffold. Electron micrographs revealed that the BMSCs and SMSCs

adhered well to the scaffold. On day 1 of cell seeding on the scaffold, the cells were able to attach firmly to the hydrogel surface through extension; after 3 days, cell proliferation on the scaffold was evident, as the cells covered more of the scaffold surface and secreted matrix; by day 5, the cells covered most of the scaffold and displayed stratified growth (Fig. 4d). The live/dead staining test indicated that the stem cells had good proliferation; on day 1 postseeding, the cells were clearly proliferating; by day 3, cell proliferation was significant; and by day 5, the cells covered the material and maintained good activity (Fig. 4e). A CCK-8 assay to detect the proliferation of stem cells on the piezoelectric scaffold revealed that on days 1, 3, and 5 of culture, cell proliferation was characterized by an increase in cell number over time, with statistically significant differences among the three time points (Fig. S4a). Notably, Hyd₆ had virtually no effect on the activity of BMSCs or SMSCs. In the hemolysis test, the hemolysis rate of all hydrogel groups was less than 5 % (Figs. S4b and c), indicating satisfactory blood compatibility.

2.3. Ultrasonic tolerance analysis *in vitro*

Before the impact of US-driven electrostimulation (ES) via KNN-Hyd on the migration and differentiation of BMSCs *in vitro* can be examined, the biosafety of ES must be assessed. As shown in Fig. 4f, BMSCs were seeded on Hyd₆ piezoelectric scaffolds within culture dishes without biochemical induction factors and were exposed to 40 kHz US treatment at various acoustic pressures (0, 50, 100, and 150 kPa) for 20 min each day. Apoptosis triggered by US-activated ES was identified through flow cytometry via the use of FITC-conjugated Annexin V as a fluorescent indicator. Fig. 4g and h shows the flow cytometry results for BMSCs following US irradiation. As shown in Fig. 4g, under US stimulation at an acoustic pressure of 150 kPa, no change in apoptosis was observed for the BMSCs cultured on both the culture dishes and the Hyd scaffolds. This outcome verified the biological safety of US. In contrast, for the BMSCs cultured on the Hyd₆ scaffolds, significantly enhanced apoptosis was observed, indicating that excessive ES driven by Hyd₆ US could induce cell apoptosis. It was discovered that wireless ES of BMSCs is secure under acoustic pressures not exceeding 100 kPa.

The effect of US-driven ES on the morphology of the BMSCs were subsequently observed via SEM. Cytoskeleton staining revealed that the cells in the control and Hyd groups under US stimulation at 150 kPa, as well as the Hyd₆ groups stimulated at 50 kPa and 100 kPa, exhibited excellent cell elongation with typical actin stress fibers (white arrows) (Fig. 4i), indicating good growth. In contrast, BMSCs in the Hyd₆ piezoelectric scaffold under US irradiation at 150 kPa all retained their spherical shape, with actin staining appearing more granular (red arrows). These findings suggest that US with an acoustic pressure exceeding 100 kPa is detrimental to the ES of BMSCs. Furthermore, we used the CCK-8 assay to detect the cell activity of BMSCs seeded on piezoelectric scaffolds under various intensities of US stimulation (Figs. S4d–f). The results also confirmed the safety of US with an acoustic pressure not exceeding 100 kPa for BMSCs. In subsequent experiments, 100 kPa was established as the safe intensity for US therapy.

2.4. *In vitro* chondrogenesis induction capacity of Hyd₆ with US treatment

Studies have indicated that piezoelectric scaffolds can enhance the *in vitro* chondrogenic differentiation and cartilage regeneration of stem cells under stress-driven conditions [12]. We hypothesize that multifunctional piezoelectric hydrogels could enhance the chondrogenic differentiation of stem cells under US-driven conditions. To validate our hypothesis, first, BMSCs and SMSCs were seeded on hydrogel scaffolds and then placed into culture dishes containing normal growth medium. After the hydrogel scaffolds were irradiated with US for 7 days, the expression of chondrogenic markers in the stem cells within the scaffolds was detected (Fig. 5a). The US treatment parameters were as follows: 40 kHz, 100 kPa, 20 min per day. We assessed the ability of US-activated piezoelectric hydrogels to increase chondrogenesis at the gene and

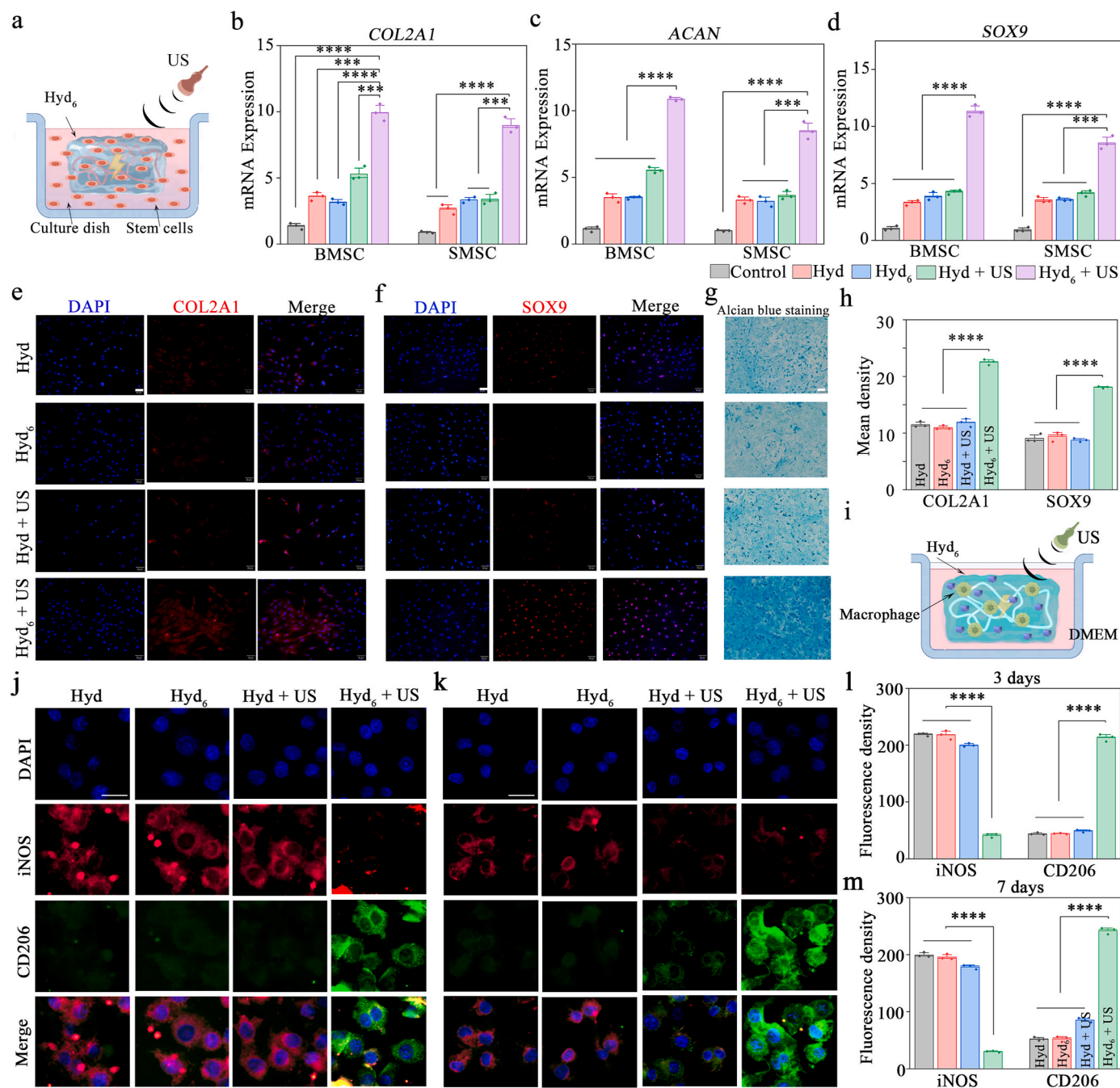


Fig. 5. Piezoelectric Hyd₆ combined with US treatment induces chondrogenesis *in vitro*. (a) Schematic diagram of the BMSCs and SMSCs seeded on Hyd₆ scaffolds combined with US (by Figdraw). (b–d) Relative gene expression of the chondrogenic gene markers *COL2A1*, *ACAN*, and *SOX9* in cultured BMSCs and SMSCs on different hydrogels after 7 days of US treatment. (e) *COL2A1* visualization with immunofluorescence (red) and nuclei (blue) after 7 days of culture of BMSCs on different hydrogels subjected to US treatment. Scale bars: 50 μ m. (f) *SOX9* visualization with immunofluorescence (red) and nuclei (blue) after 7 days of culture of BMSCs on different hydrogels subjected to US treatment. Scale bars: 50 μ m. (g) Alcian blue staining of GAGs (blue) and nuclei (pink) after 7 days of culture of BMSCs on different hydrogels subjected to US treatment. Scale bars: 50 μ m. (h) Semiquantitative analysis of the mean intensity of *COL2A1* and *SOX9*. (i) Schematic diagram of the macrophages seeded on Hyd₆ hydrogels combine with US (by Figdraw). (j) Intensity of dual iNOS/CD206 immunofluorescence staining in macrophages seeded on hydrogels and cultured for 3 days. Scale bars: 20 μ m. (k) Intensity of dual iNOS/CD206 immunofluorescence staining in macrophages seeded on hydrogels and cultured for 7 days. Scale bars: 20 μ m. (l) Semiquantitative analysis of the fluorescence intensity of iNOS/CD206 in macrophages seeded on hydrogels and cultured for 3 days. (m) Semiquantitative analysis of the fluorescence intensity of iNOS/CD206 in macrophages seeded on hydrogels and cultured for 7 days. **** $p < 0.0001$ and *** $p < 0.001$.

protein levels. The RT-qPCR results shown in Fig. 5b–d indicate that after 7 days of cell stimulation, in the Hyd₆ + US group, the expression levels of *COL2A1*, *ACAN*, and *SOX9* were elevated compared with those in the other groups. Moreover, except for the Hyd₆ + US group, the other groups presented only partial upregulation of chondrogenic marker genes, not all three genes. The findings from this study align with earlier

investigations, which demonstrated that the mere presence of piezoelectric scaffolds or the isolated application of US activation did not promote chondrogenesis [9,12]. Specifically, our results revealed that the Hyd₆ + US group markedly increased the expression of the *COL2A1*, *ACAN*, and *SOX9* genes. Consequently, we propose that the synergistic application of Hyd₆ in conjunction with US creates the optimal

environment for the enhancement of chondrogenesis.

At the protein level, type II collagen (COL2A1) serves as the primary protein within the cartilage matrix, fulfilling a crucial function in this hierarchical tissue [43]. Sox9, a transcription factor that plays a pivotal role in chondrocyte differentiation and skeletal development, is frequently characterized as the principal chondrogenic factor essential for chondrogenesis [44]. Fig. 5e, f, h and Fig. S5a, b, c show IF results for COL2A1 and SOX9 across different groups. Compared with the other groups, the Hyd₆ + US group presented increased synthesis of COL2A1 and SOX9. These results suggest that the ES produced by the Hyd₆ piezoelectric scaffold under US activation significantly influences the differentiation of stem cells into chondrogenic lineages. The results of the Alcian blue staining shown in Fig. 5g and Fig. S5d indicate that the maximum quantity of glycosaminoglycans (GAGs) in standard growth medium was synthesized in the cells cultured on the US-treated piezoelectric hydrogel. The findings clearly demonstrated that the Hyd₆ + US group produced significantly greater quantities of COL2A1 and SOX9 than the other groups lacking either the piezoelectric effect or US activation. These results suggest that the localized piezoelectric charges generated by Hyd₆ when subjected to US activation are crucial in promoting the chondrogenic differentiation of stem cells. These findings align with other published studies that utilized electrical cues to enhance the regeneration of hyaline cartilage [9,11,12,45,46].

2.5. In vitro immunomodulatory effects of Hyd₆ with US treatment

In the cartilage microenvironment, macrophages differentiate into proinflammatory (M1) and anti-inflammatory (M2) phenotypes [47].

M1 macrophages orchestrate the inflammatory response during the inflammatory phase of cartilage repair, whereas M2 macrophages play crucial roles in immune regulation and tissue remodeling [48]. Promoting the shift of macrophages from the M1 phenotype to the M2 phenotype can effectively suppress persistent inflammation and promote endogenous cartilage repair.

We cultured macrophages on piezoelectric hydrogels and subjected them to US stimulation (Fig. 5i). Macrophage polarization was evaluated by IF and RT-qPCR analysis to confirm the immunomodulatory effects of Hyd₆ *in vitro*. IF and semiquantitative analysis revealed that on days 3 and 7 of culture, the expression of the M1-associated marker iNOS was significantly increased in Hyd, Hyd₆, and Hyd + US groups. In contrast, in Hyd₆ subjected to US irradiation, iNOS expression was lower than in the other three groups, while the expression of the M2-associated marker CD206 was greater (Fig. 5j–m). RT-qPCR analysis revealed that in the US-stimulated Hyd₆ group, the expression of CD206 was significantly upregulated, whereas the expression of iNOS was downregulated (Figs. S5e and f). Additionally, the expression of the inflammation-related gene *IL-6* was significantly lower in the Hyd₆ + US group than in the other three groups (Figs. S5e and f). Notably, the Hyd₆ + US group presented the highest M2/M1 ratio (Fig. S5g), indicating that this group could modulate macrophage phenotypes, suppress inflammatory responses, and promote cartilage regeneration.

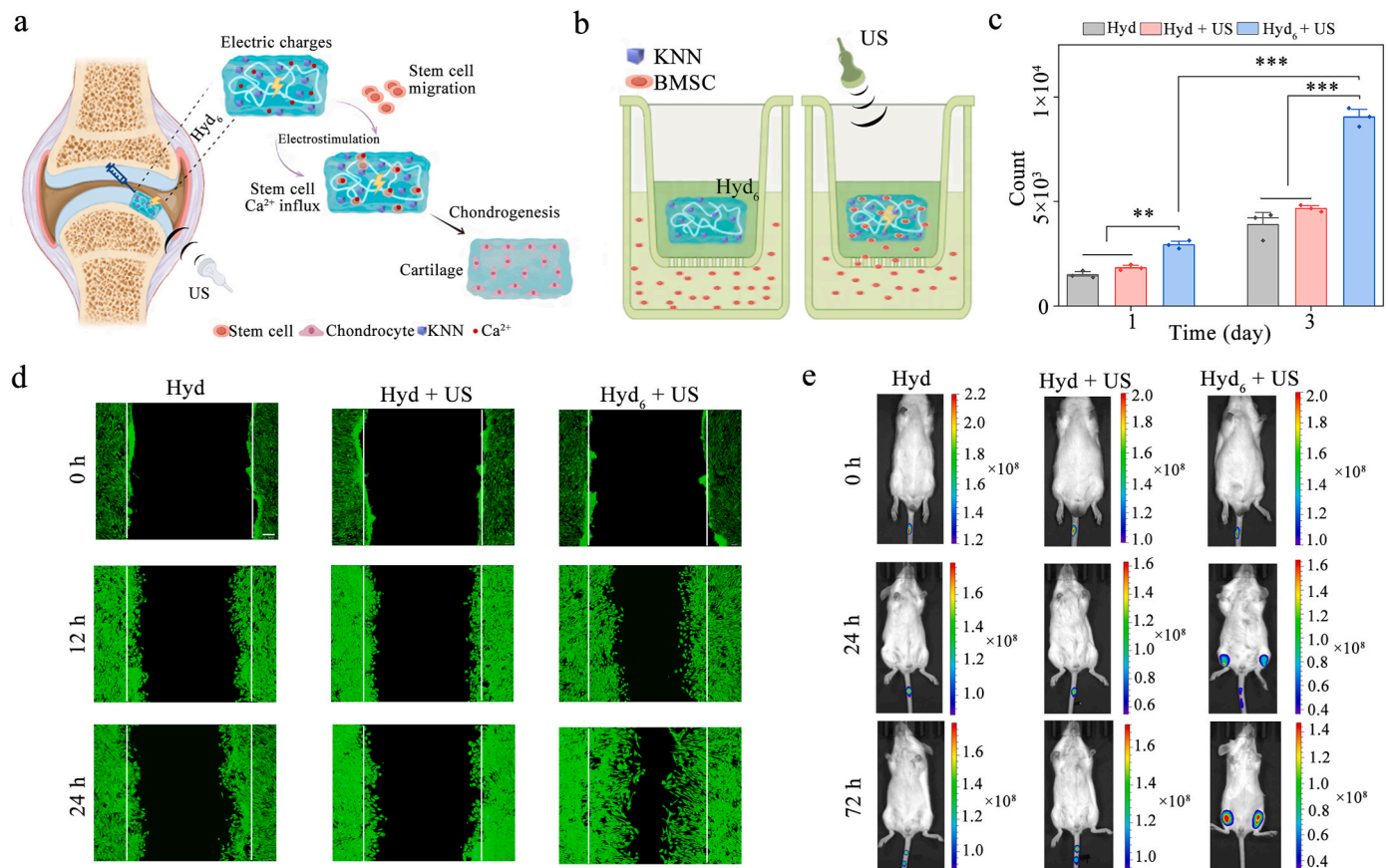


Fig. 6. Piezoelectric Hyd₆ scaffolds under US treatment recruit stem cells. (a) Schematic diagram of the hypothesis that piezoelectric Hyd₆ along with US activation recruits host stem cells and promotes Ca²⁺ influx to induce chondrogenesis (by Figdraw). (b) Schematic diagram of the process by which stem cells are recruited into a hydrogel and then treated with US in a Transwell chamber (by Figdraw). (c) Counting analysis of stem cells recruited into the hydrogel after 1 and 3 days. (d) Microscopy images of the scratch assays in different groups at 0, 12, and 24 h. Scale bars: 100 μm (e) Target aggregation analysis of DIO-labeled BMSCs *in vivo* at different times. **p < 0.01 and ***p < 0.001.

2.6. Piezoelectric hydrogels under US irradiation enhance chondrogenic differentiation by promoting the recruitment of autologous stem cells and modulating Ca^{2+} signaling

Recent studies have shown that ES enhances cartilage formation by inducing directional cell migration and promoting intracellular calcium ion influx [46]. Therefore, we hypothesize that the electrical signals generated by piezoelectric hydrogels under US irradiation might share the same mechanism (Fig. 6a). To verify our hypothesis, we investigated the effects of *in vivo* and *in vitro* cell migration, Ca^{2+} influx, and the impact of calcium channel blockers (CCBs) on chondrocyte gene markers. We utilized once more BMSCs and SMSCs as cellular models for mechanistic studies.

For cell homing, we cultured BMSCs in the lower chamber of a specially designed double-layer chamber without biochemical factors,

with piezoelectric hydrogels placed in the upper layer (Fig. 6b). After the piezoelectric scaffolds were irradiated with US for 1 and 3 days, we collected the cells recruited on the scaffolds and counted them via a flow cytometer. Fig. 6c shows the cell counts for different groups after 1 and 3 days. The Hyd₆ + US group clearly presented a greater number of stem cells, and the number of migrated cells increased with increasing treatment time. To further investigate the regulatory effects of ES on cell migration, we established an *in vitro* scratch model. BMSCs were seeded in glass-bottom dishes and cultured until a monolayer formed. Standardized pipette tips were then used to create uniform scratches in the cell monolayer, which were subsequently filled with Hyd and Hyd₆. Dynamic monitoring via a fluorescence live-cell imaging system revealed that, at the initial time point (0 h), the scratch areas were comparable across all groups (Fig. 6d). At 12 h, significant cell migration was observed in the Hyd₆ + US group, whereas the Hyd and Hyd + US

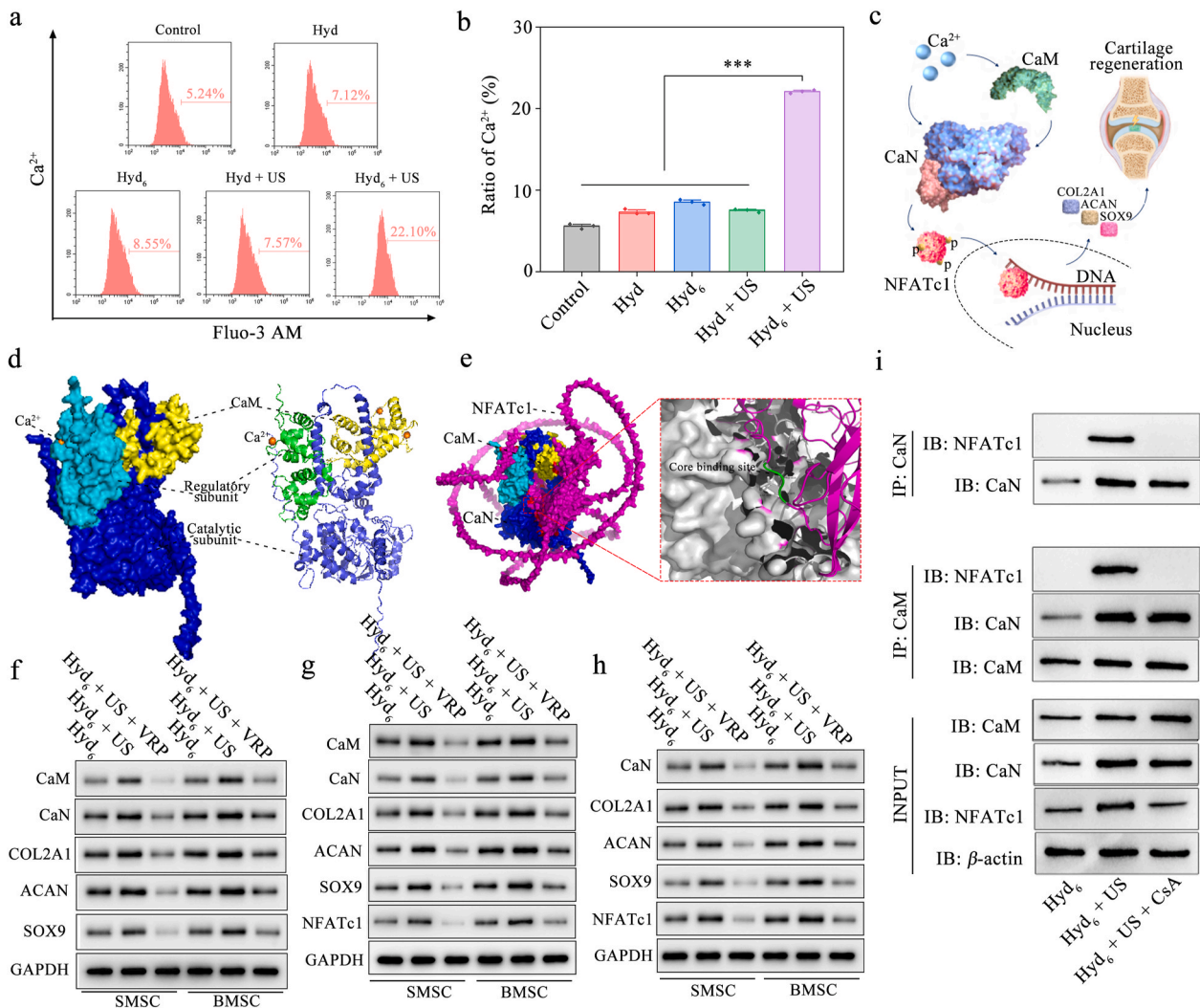


Fig. 7. Piezoelectric Hyd₆ scaffolds combined with US treatment induce chondrogenesis by activating the Ca^{2+} /CaM/CaN signaling pathway. (a) Flow cytometry detection of the intracellular calcium content in BMSCs inside the US-activated KNN-Hyd after 3 days. (b) The ratio of Ca^{2+} in the BMSCs inside the US-activated KNN-Hyd with after 3 days. (c) Schematic diagram of the hypothesis that piezoelectric Hyd₆ treated with US induces stem cells to activate the Ca^{2+} /CaM/CaN signaling pathway, thereby enhancing cartilage regeneration (by Figdraw). (d) The Ca^{2+} -CaM-CaN complex. Ca^{2+} ions are orange. CaM is yellow. The regulatory subunit of CaN is turquoise green. The catalytic subunit of CaN is blue. (e) Ca^{2+} -CaM-CaN-NFATc1 complex and its core binding site. CaM is yellow. The regulatory subunit of CaN is turquoise green. The catalytic subunit of CaN is blue. NFATc1 is expressed as a magenta color. The enlarged view on the right shows the core binding site of the complex (marked in green). (f) Relative protein expression of CaM, CaN, and the chondrogenic gene markers COL2A1, ACAN, and SOX9, respectively, in stem cells inside US-activated Hyd₆ with and without the calcium channel blocker VRP after 7 days. (g) Relative protein expression of CaM, CaN, COL2A1, ACAN, SOX9 and NFATc1 from stem cells inside US-activated Hyd₆ with and without CaM inhibitor KN-93 after 7 days. (h) Relative protein expression of CaN, COL2A1, ACAN, SOX9 and NFATc1 from stem cells inside US-activated Hyd₆ with and without CaN inhibitor FK506 after 7 days. (i) Co-IP showing the binding between CaM and CaN, and between CaN and NFATc1 in BMSCs. CaM and CaN were chosen as the bait proteins. CaM, CaN, and NFATc1 were chosen as the prey proteins. β -actin is not only an internal control but also a constituent unit of the cytoskeleton. *** $p < 0.001$.

groups exhibited only marginal migration. By 24 h, the scratch area in the Hyd₆ + US group was almost completely covered by BMSCs, whereas the other groups still retained noticeable gaps. These results demonstrate that the endogenous ES generated by the piezoelectric hydrogel upon US activation can effectively enhance the directional migration of BMSCs. Additionally, we generated chondral defects in the bilateral knees of rats and injected the same volume of Hyd₆, injecting DIO-labeled BMSCs into the rats via the tail vein. The *in vivo* imaging of Fig. 6e confirmed that most of the BMSCs were directionally aggregated in the bilateral knee joints one day after injection, with no significant fluorescence observed in other organs. These findings indicate that ES could indeed promote cell migration.

As important second messengers, intracellular Ca²⁺ plays a key role in the signal transduction of stem cell differentiation into chondrocytes [49]. Recent studies have shown that ES promotes cartilage regeneration by driving Ca²⁺ influx and activating the p38 MAPK pathway [46]. A classic study also showed that continuous ES of stem cells can drive Ca²⁺ influx, subsequently activating downstream cascade reactions and thus promoting chondrogenic differentiation [12]. Therefore, we conducted a study on Ca²⁺ influx in stem cells via flow cytometry. Fig. 7a, b illustrates that the cells cultured on the US-irradiated Hyd₆ scaffolds presented the highest Ca²⁺ content after one day of ES. Moreover, compared with the other groups, the piezoelectric scaffolds, when activated by US, significantly inhibited the expression of the inflammatory cytokine IL-6 and the cartilage matrix degradation factor MMP-13 (Figs. S6a and b). This could be attributed to the influx of Ca²⁺, which has been shown to inhibit the production of IL-6 and MMP-13 [50]. To further verify the role of Ca²⁺ influx in chondrogenesis, we used verapamil (VRP), an L-type voltage-gated CCB, to modulate the cell culture medium. Upon the addition of VRP to the culture medium, the cells ceased to express chondrogenic marker genes (Figs. S6c–e). This finding further reinforces our hypothesis that piezoelectric charges promote the chondrogenic differentiation of BMSCs through increased Ca²⁺ influx.

2.7. Piezoelectric scaffolds combined with US irradiation induce chondrogenic differentiation of stem cells via the activation of the Ca²⁺/CaM/CaN/NFATc1 signaling pathway

Calmodulin (CaM), a calcium ion sensor, can respond to changes in the intracellular calcium concentration, thereby regulating downstream signaling processes [51]. Calcineurin (CaN) is the only phosphatase activated by Ca²⁺ and CaM; it consists of catalytic subunit A and regulatory subunit B, which form a dimer [52]. The function of T-cell-related cytoplasmic nuclear factor (NFAT) relies on CaN. CaN can dephosphorylate highly phosphorylated NFAT, leading to its nuclear translocation [53]. Activated NFATc1 can promote chondrogenesis [54]. Previous studies have shown that elevated Ca²⁺ concentrations can promote cartilage formation through the activation of the NFAT axis involving CaN/nuclear factor [55]. Therefore, we hypothesize that when Ca²⁺ influxes into the cell and binds to CaM, it activates CaN. Activated CaN further promotes the dephosphorylation of NFATc1. Dephosphorylated NFATc1 then migrates to the nucleus, activating the expression of cartilage-related genes (Fig. 7c). To validate this hypothesis, we used AlphaFold3 (AF3) to predict the three-dimensional structures and interactions of CaM, CaN, and NFATc1, which were further confirmed by coimmunoprecipitation (co-IP) experiments. We also investigated the effects of CCBs, CaM inhibitors, and CaN inhibitors on chondrocyte gene markers and NFATc1.

AF3, as a state-of-the-art artificial intelligence protein structure prediction system, can comprehensively calculate the entire molecular complex and generate the most accurate structures, achieving unprecedented accuracy in predicting protein-protein interactions [56,57]. Fig. S7a shows the structural prediction of the CaN complex by AF3, which includes a catalytic subunit (blue) and a regulatory subunit (turquoise green). When Ca²⁺ (orange) is increased, the conformation of

CaN changes (Fig. S7b), suggesting that CaN might be activated by Ca²⁺. Fig. 7d displays the structural prediction after the binding of Ca²⁺ (orange), CaM (yellow), and CaN (turquoise green: regulatory subunit; blue: catalytic subunit). Fig. S7c shows the seven interaction regions after binding (red area). The conformation of CaN further changes, with the catalytic subunit spreading out. We speculate that after CaN is activated by the complex of Ca²⁺ and CaM, it might catalyze substrate dephosphorylation. Fig. 7e and Fig. S7d display the structural prediction after the binding of Ca²⁺, CaM, CaN and NFATc1 (magentas). Thus, NFATc1 clearly interacts with the catalytic subunit of CaN, which is consistent with our predicted results. The above prediction results show that pTM is greater than 0.5 and that ipTM is greater than 0.8, indicating that the overall anticipated folding of the complex may closely resemble the actual structure and that the precision of the predicted relative positions of the subunits within the complex is notably high. By predicting the structure of the Ca²⁺, CaM, and CaN complexes, we can gain a deeper understanding of our hypothesis that US-activated hydrogel scaffolds promote stem cell chondrogenic differentiation through the Ca²⁺/CaM/CaN signaling pathway.

We Subsequently used Western blotting to study the effects of ES on CaM and CaN. As shown in Fig. S7e, the piezoelectric scaffold under US stimulation led to an increase in the expression of the CaM and CaN proteins in stem cells, indicating that US-driven piezoelectric hydrogels might regulate the differentiation of stem cells toward chondrogenesis through the Ca²⁺/CaM/CaN axis. To test this hypothesis, we added CCB (VRP), a CaM inhibitor (KN-93), and a CaN inhibitor (FK506) to the culture medium. Fig. 7f shows that the piezoelectric hydrogel combined with US irradiation upregulated the expression of CaM, CaN, and chondrocyte marker proteins in stem cells, but when VRP was added, the protein expression of CaM and CaN significantly decreased, and the protein expression of the chondrocyte markers COL2A1, ACAN, and SOX9 was also significantly downregulated. These findings suggest that blocking Ca²⁺ channels might prevent stem cell differentiation into cartilage by inhibiting the expression of CaM and CaN. After KN-93 was added, the expression of CaM, CaN, and chondrocyte marker proteins was downregulated, and the expression of dephosphorylated NFATc1 also decreased (Fig. 7g). When FK506 was present, the expression of CaN, chondrocyte marker proteins, and NFATc1 proteins decreased (Fig. 7h). These results suggest that US-driven piezoelectric hydrogels might regulate the differentiation of stem cells toward chondrogenesis through the Ca²⁺/CaM/CaN/NFATc1 signaling pathway.

To further investigate whether direct interactions exist between CaM and CaN, as well as between CaN and NFATc1, co-IP experiments were performed. The results demonstrated that CaN and NFATc1 were detected in the immunoprecipitated CaM products in the BMSCs. These findings indicate that the endogenous ES generated by Hyd₆ upon US stimulation enhances intracellular Ca²⁺ signaling, thereby promoting the assembly of the CaM-CaN-NFATc1 complex, which is indicative of the activation of the Ca²⁺-dependent signaling pathway. Immunoprecipitation of CaN directly revealed the enrichment of NFATc1 in the IP products, confirming that the US-activated piezoelectric hydrogel significantly enhances the physical interaction between NFATc1 and CaN through a mechanoelectrical coupling effect. The addition of the CaN inhibitor cyclosporine A (CsA) completely abolished the dephosphorylation of NFATc1, reducing the binding strength of the CaN-NFATc1 complex to baseline levels (Fig. 7i). This result directly confirms that the interaction between CaN and NFATc1 is strictly dependent on the phosphatase activity of CaN and is catalysis dependent. These findings are highly consistent with the predicted protein interaction interface of AF3 and fully support the central hypothesis of this study: US-activated piezoelectric scaffolds regulate NFATc1 nuclear translocation via the Ca²⁺/CaM/CaN signaling axis, thereby driving the chondrogenic differentiation of stem cells (Fig. 7c). Further functional experiments revealed that the expression levels of COL2A1, ACAN and SOX9 were significantly greater in the Hyd₆ + US group than in the other groups (Figs. S7f–h), confirming the biological effects of the signaling

pathway.

2.8. Piezoelectric scaffolds combined with US promote endogenous cartilage regeneration *in vivo*

There are few reports on the use of US-driven piezoelectric scaffolds to repair damaged tissues in deep tissues, such as inside the knee joint. In this study, we created a chondral defect (diameter: 4 mm, depth: 2 mm) in the trochlear groove of the knee joint of rabbits via a trephine to evaluate the regenerative capacity of the piezoelectric scaffold under US activation. Before conducting the animal experiments, we placed the nanogenerator in the rabbit knee joint cavity. After the wound was sutured, electrical output was detected during US stimulation (Fig. S3a, Fig. 3I). These findings indicate that US can reach the cartilage defect where the Hyd₆ scaffold is implanted. The US treatment parameters remained consistent in both the *in vivo* and *in vitro* experiments (20 min per day, 40 kHz, 100 kPa, 5 days per week). After 4–8 weeks of treatment, the knees were collected and subjected to macroscopic evaluation, imaging assessment, histological evaluation, and mechanical property analysis.

The macroscopic images of the knee joint revealed that the Hyd₆ + US group had more cartilage tissue in the defect than the other groups did. At the end of week 8, the regenerated tissue in the Hyd₆ + US group integrated well with the defect margins, presenting smooth white cartilage, indicating better transparent cartilage regeneration (Fig. 8a). Additionally, the ICRS macroscopic scores revealed that, at both 4 and 8 weeks, the repair effect in the Hyd₆ + US group was significantly greater than that in the control group, with the repair level approaching that of normal cartilage (Fig. 8b).

Magnetic resonance imaging (MRI) images revealed that after 4 weeks of treatment, all the groups had newly formed cartilage, and the new regenerated tissue extended to the subchondral bone, although edema still occurred in the subchondral bone. However, after 8 weeks of treatment, the Hyd₆ + US group presented a cartilage defect filled with newly formed cartilage, with continuous new cartilage resembling normal cartilage (Fig. 8c).

We used hematoxylin-eosin (H&E) staining, Safranin O/fast green (SO/FG) staining, and immunohistochemistry (IHC) staining to study tissue morphology and collagen formation (Fig. 8d, Figs. S9a and b). The H&E staining results at 4 weeks indicated that, except for the Hyd₆ + US group, the other groups still had significant collapse in the defect area (red arrow), with the regenerated tissue being atypical transparent cartilage (blue arrow) and disorganized cell arrangement. The results at 8 weeks showed that the defect was filled with a large amount of fibrous tissue (blue arrow), indicating poor overall repair. However, the newly formed tissue in the Hyd₆ + US group integrated well with the surrounding normal cartilage (black arrow), with a cell arrangement, collagen content, and organization closer to those of normal cartilage. Safranin O/fast green staining showed that at the end of week 4, more reconstructed cartilage was found in the defects of the Hyd₆ + US group (blue arrow), but it integrated poorly with the surrounding tissue, and the joint surface was rough. At week 8, the newly formed cartilage tissue in the Hyd₆ + US group (blue arrow) fused well with the natural host tissue (black arrow), exhibiting a clear cartilage structure and chondrocyte arrangement. In contrast, the other groups predominantly developed fibrotic tissue or had separated reconstructed tissue within the cartilage defect (blue arrow). These results indicate that the Hyd₆ + US group has a significant advantage in promoting cartilage regeneration and repair, effectively improving the quality of the newly formed cartilage and its integration with surrounding tissues. IHC staining showed that the Hyd₆ + US group exhibited highly positive and uniform COL2A1, indicating the rich presence of COL2A1 protein within the defect, whereas in the other groups, COL2A1 production was minimal or not detectable. At week 8, the defect had a better collagen fiber structure, similar to that of natural tissue. In contrast, the collagen network in the other groups was disordered. The subsequent ICRS histological

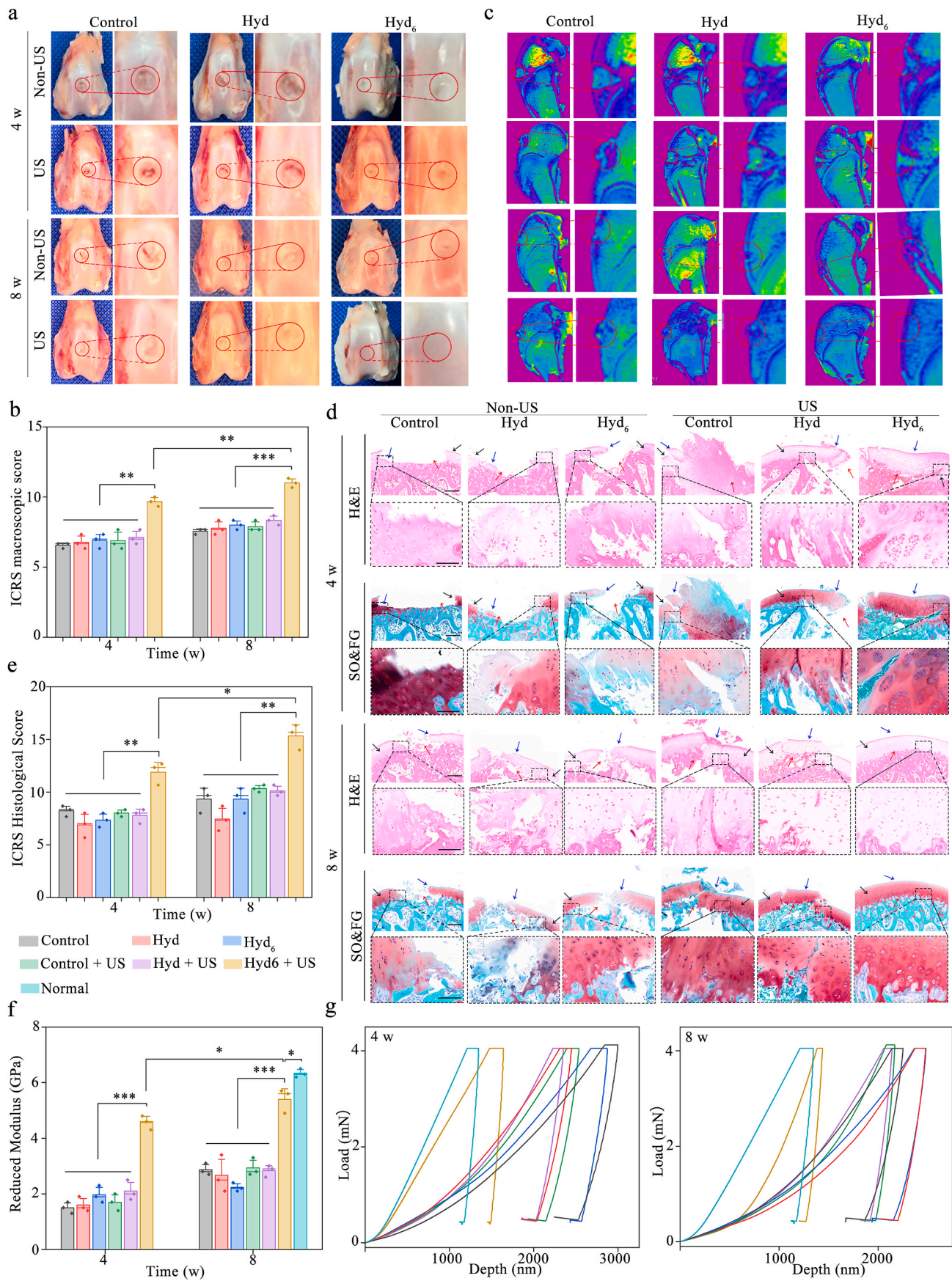
evaluation indicated that, owing to advantages in surface lubrication, matrix structure, and cell distribution and viability, the Hyd₆ + US group samples received higher scores (Fig. 8e). Histological analyses and ICRS scoring confirmed that Hyd₆ combined with US therapy significantly promoted cartilage regeneration, improving tissue integration, collagen orientation, and COL2A1 expression to a greater extent than the other treatments did.

The immunomodulatory effects of Hyd₆ under US irradiation were further validated *in vivo* (Figs. S8a–e). At week 4 after cartilage defect induction, the Hyd, Hyd₆, and Hyd + US groups presented increase expression of the M1 macrophage marker iNOS (green), indicating a proinflammatory response following hydrogel scaffold implantation. In contrast, the Hyd₆ + US group, which was subjected to US irradiation, presented significantly lower iNOS expression in the repaired tissue than the Hyd, Hyd₆, and Hyd + US groups did (Figs. S8a and c). Additionally, the expression of the M2 macrophage marker CD206 (red) was significantly greater in the Hyd₆+US repair group than in the other three groups (Figs. S8a and c). At week 8 after cartilage defect induction, similar trends were observed through IF for iNOS and CD206 (Figs. S8b and d). The expression of iNOS was lower in the US-irradiated Hyd₆ repair tissue than in the Hyd, Hyd₆, and Hyd + US groups. Moreover, the expression of CD206 was significantly greater in the US-irradiated Hyd₆ repair tissue than in the other groups (Figs. S8b and d). Similarly, the Hyd₆ + US group also presented the highest M2/M1 ratio *in vivo* (Fig. S8e), indicating that Hyd₆ under US stimulation could induce M2 polarization of macrophages *in vivo*. In summary, the multifunctional piezoelectric scaffold, which can generate high-affinity electrical signals for macrophages under US stimulation, led to a significant shift in macrophage phenotypes, promoting their transition to the M2 phenotype. These findings further highlight the potent macrophage-polarizing potential of US-driven piezoelectric hydrogels. Immunohistochemical staining of IL-6 and MMP-13, as shown in Figs. S9c and d, revealed that after 4 weeks of US stimulation, the positive cells of IL-6 and MMP-13 in the Hyd₆ + US group was decreased, similar to that in the other groups. At the 8-week time point, the positive cells of IL-6 and MMP-13 in the Hyd₆ + US group were lower than those in the other groups. These results confirmed that the piezoelectric scaffold activated by US could reduce inflammation and prevent matrix degradation by inhibiting the secretion of IL-6 and MMP-13. These findings align with recent studies demonstrating the dual role of US-activated piezoelectric materials in mitigating inflammation and promoting cartilage formation [45]. However, our results also indicate that neither piezoelectric hydrogels alone nor US stimulation alone can significantly suppress inflammation or enhance cartilage regeneration. Specifically, the *in vivo* data revealed that in the Hyd₆ + US group, the expression of inflammatory factors in the newly formed tissue at the cartilage defect site was markedly reduced, and the regenerated cartilage exhibited greater similarity to native cartilage. Thus, we further confirmed that the combined application of Hyd₆ and ultrasound stimulation represents the most effective condition for promoting cartilage formation.

Finally, we used nanoindentation technology to evaluate the mechanical properties of the reconstructed cartilage tissue. Fig. 8f displays the reduced modulus of various regenerated cartilages, comprising naturally transparent cartilage from normal tissue. The modulus values obtained from the Hyd₆ + US group after 4 and 8 weeks of US irradiation were greater than those in the other groups. Additionally, the modulus value at 8 weeks was greater than that at 4 weeks and closer to the modulus value of healthy natural cartilage. The load-displacement curve also indicated that the curve of the regenerated cartilage in the Hyd₆ + US group was similar to that of the native cartilage, indicating greater consistency (Fig. 8g).

3. Conclusion

In summary, our study explored the potential of a piezoelectric hydrogel (Hyd₆) for enhancing cartilage regeneration through US



(caption on next page)

Fig. 8. Piezoelectric Hyd₆ scaffolds combined with US promote cartilage regeneration *in vivo*. (a) Digital photographs showing the femurs of rabbits in the control, Hyd, and Hyd₆ groups with or without US activation (4–8 weeks). The red circle marks where the defect was originally created. (b) ICRS score for macroscopic cartilage evaluation with or without US activation of the knees of rabbits (4–8 weeks). (c) MR images of the femurs of rabbits in the control, Hyd, and Hyd₆ groups with or without US activation (4–8 weeks). The red circle marks where the defect was originally created. (d) H&E staining and safranin O/fast green to evaluate the newly formed articular cartilage in the control, Hyd, and Hyd₆ groups with or without US activation (4–8 weeks). Scale bars: 1 mm. Scale bar: 50 μ m (magnified image). Black arrow = normal cartilage. Blue arrow = repaired tissues. Red arrow = cartilage defects. (e) ICRS histological evaluation newly formed cartilage tissues with or without US activation in rabbit knees (4–8 weeks). (f) Reduced modulus of newly formed cartilage inside the defect in the different hydrogel groups with and without US activation (4–8 weeks). Healthy normal rabbit cartilage served as a positive control. (g) Representative indentation curves for different groups after 4 and 8 weeks of treatment. * $p < 0.05$, ** $p < 0.01$, and *** $p < 0.001$.

stimulation. The hydrogel, composed of PVA, PAA, CS, and KNN nanoparticles, exhibited multifunctional properties including injectability, self-healing capabilities, and piezoelectric characteristics. These properties synergistically facilitate the chondrogenic differentiation of stem cells, making them promising materials for cartilage repair. The fabrication and characterization of Hyd₆ revealed its excellent biocompatibility, biodegradability, and electromechanical conversion capabilities. The microstructure, mechanical properties, and swelling behavior of the hydrogel were optimized to ensure its effectiveness as a filling agent for cartilage defects. The injectability and rapid gelation of Hyd₆ allow it to conform to complex defect shapes, while its self-healing and adhesive properties ensure stability and integration with the surrounding tissue. Experiments conducted both *in vitro* and *in vivo* demonstrated that the combination of Hyd₆ and US stimulation promoted the recruitment of autologous stem cells and significantly enhanced chondrogenesis. The piezoelectric effect of Hyd₆ under US activation generates electrical signals that promote the influx of Ca^{2+} , activating downstream CaM/CaN/NFATc1 signaling pathways and accelerating cartilage formation. This mechanism was further confirmed through the use of calcium channel blockers and inhibitors, which suppressed the chondrogenic differentiation of stem cells. An *in vivo* study in a rabbit model of chondral defects revealed that Hyd₆ combined with US treatment significantly improved cartilage regeneration, as evidenced by better integration of the regenerated tissue with the surrounding cartilage, greater COL2A1 expression, and improved mechanical properties. The results highlight the potential of Hyd₆ as a novel therapeutic approach for treating cartilage injuries, offering a self-powered, noninvasive, and effective strategy for tissue engineering and regenerative medicine. Overall, this research bridges the gap in current cartilage repair strategies by integrating piezoelectric materials with US stimulation, providing a new direction for the development of more effective treatments for cartilage injuries and improving patient outcomes.

4. Experimental section

4.1. Preparation of the KNN-Hyd

First, 1 g of polyvinyl alcohol (PVA, Aladdin) was dissolved in 10 mL of deionized water, and then the mixture was stirred in a water bath at 90 °C for 3 h to achieve a transparent solution. Then, the KNN nanoparticles (Qijin New Material Company, Quanzhou) were weighed, added to 0.85 mL of acrylic acid solution (AA, Klamar), and stirred with a magnetic stirrer for 30 min, followed by ultrasonic treatment for 30 min to ensure uniform dispersion of the KNN nanoparticles. Next, 0.5 g of chitosan (CS, McLean) was added to a mixed solution of 1 mL acetic acid (Aladdin) and 10 mL water, and the mixture was stirred with a magnetic stirrer until completely dissolved. After that, the PVA, PAA, and CS solutions were mixed, add 0.01 g of $\text{N,N}'$ -methylenebisacrylamide (BIS, Sigma) was added, and the mixture was stirred for 30 min. Then, 0.5 mL of 10 mol/L NaOH (Sigma) solution was added, and the mixture was stirred for another 30 min. Next, 100 μ L of the catalyst tetramethylethylenediamine (TEMED, Sigma) was added, and the mixture was stirred for 15 min. Finally, 0.1 g of the initiator potassium persulfate (KPS, Merck KGaA) was added, and the mixture was stirred for 30 min. The pregel was placed in a mold, frozen at -18°C for 18 h, and then thawed for 8 h. This process was repeated 3 times to

obtain the PVA/PAA/CS/KNN (KNN-Hyd_x) composite hydrogel, where x represents the mass concentration of KNN.

4.2. Characterization of the KNN nanoparticles

Scanning electron microscopy (SEM, Ultra Plus, Zeiss, Germany) was used to characterize the morphology of the lyophilized hydrogels. The samples were lyophilized before SEM energy dispersive X-ray spectroscopy (SEM-EDS) analysis. The size and morphology of the KNN nanoparticles were analyzed through transmission electron microscopy (TEM, JEM-2100, JEOL, Japan). An X-ray diffractometer (XRD, D8-Discover, Bruker, Germany) was used to determine the crystalline phases of the KNN nanoparticles.

4.3. Characterization of the KNN-Hyd

XRD was also used to determine the crystalline phases of the composite piezoelectric scaffolds. A Fourier-transform infrared (FTIR) spectrometer (Nicolet iS10, Thermo Scientific, US) was used to investigate the chemical structures of the reaction products.

4.4. Swelling ratio test

An *in vitro* swelling test was employed to evaluate the swelling ratio and stability of the KNN-Hyd scaffolds. First, the solidified hydrogels (3 wt%, 6 wt%, and 9 wt% for KNN) were dried under vacuum overnight to produce dried scaffolds. The dried hydrogels were subsequently weighed (W_0) and immersed in $1 \times \text{PBS}$ ($\text{pH} = 7.4$) at 37 °C. At each predetermined time interval, the samples were weighed (W_t), and the swelling ratio was determined via the following formula:

$$\text{Swelling ratio (\%)} = \frac{W_t - W_0}{W_0} \times 100\% \quad (1)$$

4.5. Rheological testing and injectability

The rheological properties of KNN-Hyd were determined with a TA rheometer (DHR-2). A 500 μ L aliquot of the KNN-Hyd precursor mixture was positioned between parallel plates, each with a diameter of 20 mm, and the gap height was adjusted to 500 μ m. The stiffness of the KNN-Hyd was evaluated via a time sweep test at a constant frequency of 1 Hz, with a deformation of 1 %, and the plate was set at 37 °C. The shear-thinning behavior of Hyd₆ was assessed. The shear rate was varied between 0.1 and 50 rad/s. To investigate the solidification time of Hyd₆, the strain was set at 10 % with a frequency of 1 Hz.

4.6. Self-healing behavior

The self-healing capacity of KNN-Hyd₆ was assessed through rheological recovery. Initially, a strain amplitude sweep test was performed over a strain range of 0.1 %–1000 % to determine the maximum critical strain that the scaffold could withstand. The self-healing properties of an unaltered hydrogel were subsequently investigated by performing alternating strain scans at a constant angular frequency of 10 rad/s. The amplitude oscillation strain was gradually increased from a small strain of 1 % to a large strain of 500 %, with each strain test separated by a 200

s interval, and this process was repeated for 3 cycles.

4.7. Adhesive ability

The bonding strength was assessed through a lap-shear test. In summary, the KNN-Hyd preliminary solutions were applied to the surface of a slide, and a weight was subsequently affixed to the solution (contact area: 1 cm × 1 cm). The adhesive strength was ultimately determined via an electronic universal testing machine (CMT5105, MTS, China) fitted with a 100 N load cell at a rate of 2 mm/min.

4.8. Piezoelectric properties

A ferroelectric testing system (TRI-Multiferroic 4 kV, Radiant Technologies Inc, US) was utilized to assess the polarization-electric field (P-E) hysteresis loops of KNN-Hyd. A quasistatic d_{33} tester (SA1303A, ShiAo Instruments, China) was employed to determine the piezoelectric coefficient (d_{33}) of the dried KNN-Hyd. The amplitude of the piezoelectric signal and the hysteresis (sample bias from −4 to 4 V) were measured via piezoresponse force microscopy (PFM, MFP-3D-SA, Asylum Research, US).

4.9. Biodegradability

The degradation process of the KNN nanoparticles was examined in saline over a duration of 12 weeks. First, 0.1 g of KNN nanoparticles was immersed in 10 mL of saline at 37 °C. The mixed mixture was subjected to centrifugation (5000 rpm, 5 min) to obtain the supernatant, which was then resuspended in 10 mL of saline at 37 °C. The samples were collected on a weekly basis. Subsequently, ICP-OES (SPECTROBLUE, SPECTRO, Germany) was used to examine the concentrations of Nb^{5+} , Na^+ , and K^+ in the supernatant.

The mass reduction from the hydrogels was determined by computing the difference in mass, and the percentage of weight loss for each sample was calculated via the following equation:

$$\text{Weight loss (\%)} = \frac{W1 - W2}{W1} \times 100\% \quad (2)$$

The original weight ($W1$) of Hyd₆ was measured after vacuum drying. Each dried sample (0.1 g) was subsequently submerged in 20 mL of saline at 37 °C in a conical tube. The saline was refreshed on a weekly basis. At the end of every 4-week period, the remaining Hyd₆ samples were collected, rinsed with deionized water, and dried under vacuum. Thereafter, their final weight ($W2$) was determined. Hyd (PVA/PAA/CS hydrogel) as a control.

SEM was used to characterize the morphology of Hyd₆ after vacuum drying at the end of each month.

4.10. Hemolysis assay

One milliliter of normal rabbit fresh whole blood with anticoagulant was diluted in 10 mL of saline. The samples (Hyd₆, Hyd) were subsequently incubated in 10 mL of saline supplemented with 200 μL of diluted blood at 37 °C for 2 h. The samples were subsequently centrifuged at 2000 g/min for 10 min, after which the supernatant was transferred to a 96-well plate, after which the absorbance at 540 nm was measured. Deionized water served as the positive control, whereas saline served as the negative control. The hemolysis rate (%) was calculated as follows:

$$\text{Hemolysis rate (\%)} = \frac{S - \text{NC}}{\text{PC} - \text{NC}} \times 100\% \quad (3)$$

where S denotes the absorbance value of the samples, NC represents the absorbance value of the negative controls, and PC indicates the absorbance value of the positive controls.

4.11. Fabrication of a nanogenerator made of KNN-Hyd

To detect the electrical output capability of KNN-Hyd, a nanogenerator was constructed.

Au electrodes were applied to the two surfaces of the KNN-Hyd (3 wt %, 6 wt% and 9 wt% for KNN), followed by the use of two Cu wires to establish electrical connections for the KNN-Hyd nanogenerators. Subsequently, polyethylene terephthalate (PET) films were implemented to encapsulate and provide a waterproof barrier, ensuring insulation and safeguarding of the KNN-Hyd devices.

4.12. Electrical signal generation ability

Additionally, a self-built detection system was established for recording the output voltage and current. The US excitation equipment was constructed according to the literature [38]. The homemade equipment was composed of a US excitation device, a lectrostatic tester (FMX-003, STATIC, Japan), a digital storage oscilloscope (4828, Pico Technology, UK), a picoammeter (6514, Keithley, US), and a linear power amplifier (Model LA-200, Raymax Company, Switzerland). The custom-built detection system was employed to monitor the fluctuations in the output voltage and current of the nanogenerator when subjected to external periodic high-frequency US impacts (40 kHz).

For *in vivo* electrical output exploration, the nanogenerator (made of Hyd₆) was implanted into the medial compartment of the rabbits' knees after anesthesia and shaving. US irradiation (40 kHz) of the knees of the rabbits was then performed, and the output voltage and current were recorded via homemade equipment. For *in vitro* electrical output measurements, the nanogenerator was directly connected to homemade equipment, and the output voltage and current were recorded following ultrasound irradiation.

4.13. Cell culture and biocompatibility

Rabbit BMSCs (RBXMX-01001, Cyagen) and mouse SMSCs (CYM00126, EnkiLife) were used to assess the cytotoxicity of the hydrogel *in vitro*. The cells were cultured in growth medium following the manufacturer's instructions and then seeded onto the Hyd₆. SEM was used to observe the cell morphology. A Cell Counting Kit-8 (CCK-8, KGO1110-1, KeyGEN) was used for cell proliferation evaluation in accordance with the product specifications. The cells on the scaffolds were subsequently stained via a live/dead cell double-staining kit (calcein-AM/propidium iodide, Sigma) to assess cell viability on days 1, 3, and 5. All fluorescence images were captured and observed via a microscope (DMI8, Leica).

4.14. Cell tolerance analysis with US irradiation *in vitro*

To assess the biocompatibility of US-activated ES using the KNN-Hyd substrate, BMSCs were grown on the Hyd₆ scaffolds as well as on the Hyd and Control (no hydrogel) surfaces for 5 days. These cells were subsequently subjected to US treatment at 40 kHz frequency with varying acoustic pressures of 0, 50, 100, and 150 kPa, each for a duration of 20 min. Apoptosis was identified through flow cytometric analysis via the use of Annexin V, which was tagged with FITC to serve as a fluorescent marker. A CCK-8 (KGO1110-1, KeyGEN) was used to evaluate cell proliferation and activity.

To study how the morphology of BMSCs is regulated by US irradiation, 2×10^4 BMSCs/mL were cultured on Hyd₆, Hyd, or the control for 5 days. The samples were subsequently rinsed, fixed, washed, and stained with FITC-phalloidin (1:100, ab235137, Abcam) and DAPI (1:100, ab104139, Abcam). FITC-phalloidin (red) and nuclei (blue) on the scaffolds were examined via fluorescence microscopy (CKX53, Olympus).

4.15. Analysis of anti-inflammatory effects on macrophage polarization *in vitro* and *in vivo*

Bone marrow-derived macrophages were extracted from 8-week-old male Sprague–Dawley rats and cultured at a density of 5×10^5 cells per well in DMEM supplemented with macrophage colony-stimulating factor (M-CSF, 40 ng/mL) for 1 week. Subsequently, 4×10^5 cells were seeded in 24-well plates and activated with 10 ng/mL IL-1 β for 24 h. Hyd and Hyd₆ were then added to the culture medium and cocultured with the activated cells. US irradiation was applied according to the group allocation, with the following parameters: 40 kHz, 100 kPa, 20 min per day. After 3 and 7 days of activation, the cells were washed with PBS. For iNOS and CD206 immunofluorescence staining, the samples were incubated with primary antibodies (iNOS: 1:500, bs-0162r, Bioss; CD206: 1:200, bs-0162r, Bioss). The secondary antibodies (goat anti-mouse Alexa Fluor 488, Abcam) were applied at a 1:100 dilution and incubated for 1 h at room temperature. The nuclei were counterstained with 4',6-diamidino-2-phenylindole (DAPI) after washing with PBS, and the samples were examined via a fluorescence microscope (Nikon, Tokyo).

To evaluate the immunomodulatory effects of Hyd₆ under US stimulation *in vivo*, 24 male *New Zealand white rabbits* (weighing ~3 kg; Hengtai Laboratory Animal Breeding Co., Ltd., Wuxi, China) were randomly assigned to four groups: Hyd, Hyd₆, Hyd + US, and Hyd₆ + US. After anesthesia, bilateral chondral defects (4.0 mm in diameter and approximately 2 mm in depth, located in the femoral trochlea) were created in the knees of the rabbits. The hydrogels were then injected into the defect sites. Following the solidification of the hydrogel within the defect, the patella was repositioned and the joint was sutured closed. The rabbits were allowed free movement and ad libitum feeding post-surgery and were subjected to US stimulation according to their group assignments (parameters: 40 kHz, 100 kPa, 20 min per day). On post-operative weeks 4 and 8, the rabbits from each group were euthanized, and the scaffolds were retrieved. Macrophage polarization *in vivo* was assessed by immunofluorescence staining, and images were acquired via confocal laser scanning microscopy. Quantitative analysis was subsequently performed via ImageJ software.

4.16. RNA isolation and qRT-PCR

The expression levels of chondrogenesis-related genes (COL2A1, ACAN, and SOX9), IL-6, and MMP-13 were analyzed via RT-qPCR. For the chondrogenesis induction study, BMSCs and SMSCs were seeded on hydrogel scaffolds and divided into groups without US stimulation (Hyd and Hyd₆) and groups with US stimulation (Hyd + US and Hyd₆ + US), with the control serving as the blank control. For mechanistic research, BMSCs were seeded on Hyd₆ scaffolds and divided into 3 groups: Hyd₆, Hyd₆ + US, and Hyd₆ + US + VRP (calcium channel blocker, verapamil, 50 μ M; HY-14275, MedChemExpress). The Hyd₆ + VRP group was added for MMP-13 detection. For functional assays, the samples were divided into 3 groups: Hyd₆, Hyd₆ + US, and Hyd₆ + US + CsA (cyclosporin A, 10 μ g/ml, ab120114, Abcam). The cells on scaffold were collected after 7 days of treatment with US irradiation in a culture dish containing normal medium. US parameters: 40 kHz, 100 kPa, 20 min per day, for 7 consecutive days. Rat bone marrow-derived macrophages were seeded at a density of 1×10^6 cells per well in 12-well plates containing Hyd or Hyd₆, with three wells per group. The cells were cultured in DMEM containing 10 ng/mL IL-1 β for 3 days and subjected to US stimulation according to the group (40 kHz, 100 kPa, 20 min per day). Total RNA was isolated from stem cells via Trizol RNA isolation reagent (KGF5101-100, KeyGEN). The RNA was transformed into cDNA via a One-Step RT-PCR Kit (KGF2107-100, KeyGEN). RT-qPCR was subsequently conducted to target various genes. GAPDH was used as the reference gene. The outcomes were analyzed via the comparative cycle-threshold method, and all the primers used are listed in Table S2.

4.17. Immunofluorescence staining and alcian blue staining

At 7 days, the hydrogels were dehydrated through a series of graded alcohol solutions, decalcified, embedded in wax, and then sectioned for staining.

For COL2A1 and SOX9 immunofluorescence staining, the scaffolds were washed and incubated. Then, the samples were incubated with an antibody (COL2A1: 1:500, ab34712, Abcam. SOX9: 1:200, ab185230, Abcam). Alexa Fluor 594-labeled goat anti-rabbit IgG (1:500, ab150080, Abcam) was used as the secondary antibody.

Then, the slides were soaked in Alcian blue staining solution, followed by a counterstaining period with nuclear fast red.

4.18. Assessment of cell recruitment

A transwell chamber assay was used to evaluate the capacity of US-irradiated hydrogels to recruit stem cells. The hydrogel was placed in the upper chamber of the Transwell insert, with the BMSCs seeded in the lower chamber, and the two layers of culture medium were separated by a polycarbonate membrane (8.0 μ m). The hydrogel in the upper chamber was subjected to US irradiation for 1 and 3 days. The cells from the hydrogels of each group were extracted, prepared into a single-cell suspension, and then counted via a flow cytometer (LSRFortessa X-20, BD Biosciences). The US irradiation parameters were as follows: 40 kHz, 20 min per day.

BMSCs were seeded in glass-bottom cell culture dishes (150682, Thermo Fisher Scientific) and cultured until complete confluence was achieved under standard conditions of 37 °C and 5 % CO₂. A sterile 200 μ L pipette tip was used to apply constant pressure perpendicular to the surface of the dish, creating a uniform linear scratch across the cell monolayer. The original culture medium was then removed, and the cells were gently washed three times with prewarmed (37 °C) 1 \times PBS (5 mL each time, with a dwell time of 30 s) to thoroughly remove detached cell debris. Precisely 200 μ L of precooled (4 °C) Hyd or Hyd₆ hydrogel precursor solution was injected into the scratch area to ensure complete coverage of the scratch interface. The dishes were then incubated at 37 °C for 30 min to allow the hydrogel to solidify and form a stable three-dimensional structure, after which 2 mL of fresh complete culture medium was added. The dishes were placed in a live-cell imaging system for continuous culture for 24 h. One hour before the end of the experiment, 5 μ M calcein-AM live-cell fluorescent dye was added, and the cells were incubated in the dark. Fluorescence images of the scratch area were captured via a confocal microscopy.

For *in vivo* cell recruitment assessment, 24 male Sprague-Dawley rats (200–220 g, Sippr B&K Laboratory Animal Ltd., Shanghai, China) were randomly assigned to 3 groups: the control (Hyd), Hyd₆, and Hyd₆ + US groups. Chondral defect surgery was conducted on both knees of the animals following anesthesia. The hydrogels were then injected into the defect area. Upon solidification of the hydrogel within the defect, the joint was sutured closed. The BMSCs were labeled with DIO and then injected through the tail vein after model establishment. Treatments were administered to each knee, with US irradiation lasting 20 min per day (40 kHz, 100 kPa). Then, *in vivo* fluorescence images were taken on the 1st day and 3rd day after US stimulation with a small animal *in vivo* optical imaging system (IVIS Spectrum, PerkinElmer, US).

4.19. Ca²⁺ content analysis

Flow cytometry was used to assess the calcium ion content of that BMSCs in each group. After the BMSCs were cultured on Hyd₆ treated with US for 1 day, they were rinsed with PBS (ab90220, Abcam), collected and a single-cell suspension was prepared. The cells were stained with the calcium indicator Fluo-3AM (ab145254, Abcam), incubated, washed, and then subjected to machine detection (LSRFortessa X-20, BD Biosciences).

4.20. Western blot analysis

A Western blot analysis was used to detect the expression of chondrogenesis-related protein markers (COL2A1, ACAN, and SOX9) and signaling pathway proteins (CaM, CaN, and NFATc1) in the stem cells of each group. The cells (BMSCs and SMSCs) on the scaffold were collected after 7 days of treatment with US irradiation in a culture dish containing normal medium. US parameters: 40 kHz, 100 kPa, 20 min per day, for 7 consecutive days. In each group of culture media, CCBs containing VRP (verapamil, 50 μ M, HY-14275, MCE), CaM inhibitors (KN-93, 0.37 μ M, ab145638, Abcam), and CaN inhibitors (FK506, 0.056 nM, ab120223, Abcam) were added. For the Co-IP experiments, 3 groups were established: Hyd₆, Hyd₆ + US, and Hyd₆ + US + CsA. Proteins were extracted via RIPA lysis buffer (KeyGEN) and subsequently separated via 10 % SDS-PAGE (KeyGEN). Western blotting was performed with primary antibodies against COL2A1 (1:1000, ab34712, Abcam), ACAN (1:1000, ab3778, Abcam), SOX9 (1:1000, ab185230, Abcam), CaM (1:1000, ab22552, Abcam), CaN (1:1000, ab124831, Abcam), and NFATc1 (1:1000, ab21510, Abcam). Peroxidase-conjugated goat anti-rabbit IgG (1:5000, ab6721, Abcam) served as the secondary antibody.

4.21. AlphaFold3 prediction of CaM-CaN interaction

The amino acid sequences of CaM [58], CaN [59] and NFATc1 [60, 61] were obtained, the AlphaFold server (<https://alphafoldserver.com/>) was used, and the data were uploaded for analysis.

4.22. Animal model and histological analysis

A full-thickness chondral defect rabbit model (*New Zealand white rabbits*, weighing ~3 kg, male, Hengtai Laboratory Animal Breeding Co., Ltd., Wuxi, China) was utilized to assess the impact of KNN-Hyd combined with US irradiation on chondral defect healing. Thirty-six rabbits were randomly assigned to six groups: the control (PBS), Hyd, Hyd₆, Control + US, Hyd + US, and Hyd₆ + US groups (18 rabbits in each of the 4-week and 8-week treatment groups, with 4 legs in each group) for *in vivo* experiments. Briefly, a round chondral defect (diameter: 4 mm, depth: 2 mm) was made in the trochlear groove of the femur of the rabbits via a ring drill following anesthesia and shaving. Thirty microliters of Hyd₆, Hyd, or PBS was then injected into the defect area. Next, once the hydrogel had hardened within the defect, the joint was sutured. 2 weeks after the operation, interventions were performed on each knee, with daily US irradiation lasting for 20 min (40 kHz, 5 days/week, 4 weeks or 8 weeks).

To assess cartilage regeneration, the femurs of the knee were harvested at various time points after treatment and for morphological evaluation, radiological assessment, and histological analysis.

For morphological evaluation, pictures of the distal femoral coronal plane were taken, and the assessment of cartilage regeneration morphology was independently carried out by professionals with expertise and experience in cartilage histology. The assessment was conducted utilizing the ICRS criteria for the macroscopic examination of cartilage.

For MRI assessment, each rabbit from the 6 groups was examined for newly formed cartilage tissues via MRI analysis on a 7.0 T MRI scanner (BioSpec 70/20 USR, BRUKER) at 4 and 8 weeks postoperation, and a small animal-specific knee coil (≥ 8 channel coils, Chenguang Medical Technologies Co., Ltd., Shanghai) was used to improve the signal-to-noise and contrast-to-noise ratios. Parameters: TR-15.0 ms, TE-2.24 ms, average-1, FOV-60 mm, matrix-192 \times 192, slice thickness-3.0 mm, number of slices-22.

For histological assessment, the samples were first dehydrated in graded alcohol, decalcified, embedded in wax before sectioning, and finally sectioned for H&E and safranin O staining.

4.23. Immunohistochemistry analysis

Following 4–8 weeks of treatment, the knees of the rabbits were harvested and preserved in 10 % neutral-buffered formalin. The samples were subsequently dehydrated via a graded alcohol series and decalcified. Prior to sectioning, the samples were embedded in paraffin wax. The samples were ultimately sectioned for immunohistochemical staining ab34712 (1:100, Abcam) for COL2A1.

4.24. Biomechanical testing

A nanoindentation apparatus (TI-750 L, Hysitron) was employed to assess the mechanical characteristics of the novel cartilage form. In this investigation, the diamond Berkovich was utilized and calibrated on the reference surface prior to each trial. Parameter: 5 mN for the target strain rate and 0.3/s for strain rate [9]. Normal rabbit knees were used as a positive control.

4.25. Statistical analysis

All the results are presented as individual data points or as box plots accompanied by these data points, expressed in terms of means \pm SDs. The sample size was specified to indicate the specificity of each test conducted. Statistical significance was determined via one-way ANOVA or t-tests as appropriate, with analyses performed via GraphPad Prism 9. The exact *p*-values are documented in the Source Data file. The thresholds for significance were established at **p* < 0.05, ***p* < 0.01, ****p* < 0.001, and *****p* < 0.0001.

CRediT authorship contribution statement

Yu-Bao Liu: Writing – original draft, Validation, Resources, Methodology, Funding acquisition, Formal analysis, Conceptualization. **Xu Liu:** Writing – original draft, Software, Methodology, Conceptualization. **Xiao-Fei Li:** Writing – original draft, Validation, Resources, Methodology, Formal analysis, Conceptualization. **Liang Qiao:** Writing – original draft, Software, Methodology, Conceptualization. **Hao-Liang Wang:** Visualization, Methodology, Data curation. **Yue-Fu Dong:** Resources, Data curation. **Feng Zhang:** Resources. **Yang Liu:** Visualization, Methodology, Data curation. **Hao-Yang Liu:** Resources, Funding acquisition, Data curation. **Ming-Liang Ji:** Resources. **Lan Li:** Project administration, Funding acquisition, Conceptualization. **Qing Jiang:** Writing – review & editing, Supervision, Funding acquisition. **Jun Lu:** Writing – review & editing, Supervision, Project administration, Funding acquisition.

Data and materials availability

All the data needed to evaluate the conclusions in the paper are presented in the paper and/or the Supplementary Materials. Additional data related to this paper may be requested from the authors.

Ethics approval and consent to participate

The animal experiments in this study were conducted in accordance with the ARRIVE (Animal Research: Reporting of In Vivo Experiments) guidelines, the operating guidelines of the Animals (Scientific Procedures) Act 1986, and the National Institutes of Health's Guide for the Care and Use of Laboratory Animals. The experimental protocol was reviewed and approved by the Laboratory Animal Ethics Committee of Southeast University (approval number: 20250213001). All efforts were made to minimize the suffering of the animals during the experiments.

For the *in vivo* experiments involving rabbits and rats, the following ethical considerations were strictly adhered to.

1. The number of animals used was minimized to the extent possible while still achieving statistically significant results.
2. The animals were housed in a controlled environment with appropriate temperature, humidity, and lighting conditions, and were provided with adequate food and water.
3. The surgical procedures were performed under general anesthesia to ensure that the animals did not experience pain or distress during the operations.
4. Post-operative care was provided to monitor the animals' recovery and to manage any potential complications.
5. The animals were observed daily for any signs of discomfort or distress, and appropriate measures were taken to alleviate any suffering.
6. At the end of the experiments, the animals were euthanized using a method that was quick and humane, in accordance with the recommendations of the Laboratory Animal Ethics Committee of Southeast University.

By adhering to these ethical guidelines and obtaining the necessary approvals, we ensured that the research conducted in this study was carried out in a responsible and ethical manner, respecting the welfare of the animals and the integrity of the biological materials used.

Declaration of competing interest

In the manuscript entitled “Multifunctional piezoelectric hydrogels under ultrasound stimulation boosts chondrogenesis by recruiting autologous stem cells and activating $\text{Ca}^{2+}/\text{CaM}/\text{CaN}$ signal pathway”, the authors declare that there are no competing financial and/or non-financial interests associated with the work described. All authors involved in this study have adhered to the relevant ethical guidelines, ensuring the independence and objectivity of the research.

Specifically, this research has not been influenced by any commercial or personal interests that could affect the interpretation or reporting of the study results. The authors have no stocks or ownership interests related to this research, nor have they received any remuneration, funding, or any form of compensation for conducting, designing, or reporting the research. Furthermore, the authors have no affiliations with any organizations or entities that may benefit or be adversely affected by the results of this study.

We further declare that the results reported in this study are accurate and have not been subjected to any form of manipulation or selective reporting to conform to any specific outcomes or conclusions. The authors assume full responsibility for the integrity and impartiality of the research.

All individuals listed as authors have reviewed this statement and confirm its accuracy and completeness.

Acknowledgements

This study was supported by the National Natural Science Foundation of China (Grant nos. 81902197, 82202776, 82272557, 32422043, 32271408, and 92368201), the Natural Science Foundation of Jiangsu Province (BK20232023), the Medical Scientific Research Project of Health Commission of Nanjing city (Grant no. YKK22234), the Post-graduate Research & Practice Innovation Program of Jiangsu Province (SJCX23-0091), We also appreciate the support of the SEU Innovation Capability Enhancement Plan for Doctoral Students (CXJH-SEU 24224) and Zhongda Hospital Affiliated to Southeast University, Jiangsu Province High-Level Hospital Pairing Assistance Construction Funds (zdlyg06) and Jiangsu Province High-Level Hospital Construction Funds (GSP-LCYJFH04). Part of this work was supported by the Outstanding Young and Middle-aged Talents award (Nanjing) to Spectrum.

Appendix A. Supplementary data

Supplementary data to this article can be found online at <https://doi.org/10.1016/j.bioactmat.2025.04.009>.

References

- [1] S. Muthu, J.V. Korpershoek, E.J. Novais, G.F. Tawy, A.P. Hollander, I. Martin, Failure of cartilage regeneration: emerging hypotheses and related therapeutic strategies, *Nat. Rev. Rheumatol.* 19 (7) (2023) 403–416, <https://doi.org/10.1038/s41584-023-00979-5>.
- [2] H. Abu Owida, Recent biomimetic approaches for articular cartilage tissue engineering and their clinical applications: narrative review of the literature, *Adv. Orthop.* 2022 (2022) 8670174, <https://doi.org/10.1155/2022/8670174>.
- [3] Y. Fujii, L. Liu, L. Yagasaki, M. Inotsume, T. Chiba, H. Asahara, Cartilage homeostasis and osteoarthritis, *Int. J. Mol. Sci.* 23 (11) (2022) 6316, <https://doi.org/10.3390/ijms23116316>.
- [4] S.M. Eisenstein, B. Balain, S. Roberts, Current treatment options for intervertebral disc pathologies, *Cartilage* 11 (2) (2022) 143–151, <https://doi.org/10.1177/1947603520907665>.
- [5] K.C. Li, Y.C. Hu, Cartilage tissue engineering: recent advances and perspectives from gene regulation/therapy, *Adv. Healthcare Mater.* 4 (7) (2015) 948–968, <https://doi.org/10.1002/adhm.201400773>.
- [6] S. Chen, P. Zhu, L. Mao, et al., Piezocatalytic medicine: an emerging frontier using piezoelectric materials for biomedical applications, *Adv. Mater.* 35 (25) (2023) e2208256, <https://doi.org/10.1002/adma.202208256>.
- [7] A. Nain, S. Chakraborty, S.R. Barman, et al., Progress in the development of piezoelectric biomaterials for tissue remodeling, *Biomaterials* 307 (2024) 122528, <https://doi.org/10.1016/j.biomaterials.2024.122528>.
- [8] Z. Zhou, J. Zheng, X. Meng, F. Wang, Effects of electrical stimulation on articular cartilage regeneration with a focus on piezoelectric biomaterials for articular cartilage tissue repair and engineering, *Int. J. Mol. Sci.* 24 (3) (2023) 1836, <https://doi.org/10.3390/ijms24031836>.
- [9] T. Vinikoor, G.K. Dzidotor, T.T. Le, et al., Injectable and biodegradable piezoelectric hydrogel for osteoarthritis treatment, *Nat. Commun.* 14 (1) (2023) 6257, <https://doi.org/10.1038/s41467-023-41594-y>.
- [10] R. Langer, J.P. Vacanti, Tissue engineering, *Science* 260 (5110) (1993) 920–926, <https://doi.org/10.1126/science.8493529>.
- [11] D. Liu, X. Wang, C. Gao, et al., Biodegradable piezoelectric-conductive integrated hydrogel scaffold for repair of osteochondral defects, *Adv. Mater.* 36 (45) (2024) e2409400, <https://doi.org/10.1002/adma.202409400>.
- [12] Y. Liu, G. Dzidotor, T.T. Le, et al., Exercise-induced piezoelectric stimulation for cartilage regeneration in rabbits, *Sci. Transl. Med.* 14 (627) (2022) eabi7282, <https://doi.org/10.1126/scitranslmed.abi7282>.
- [13] C. Li, S. Zhang, Y. Yao, et al., Piezoelectric bioactive glasses composite promotes angiogenesis by the synergistic effect of wireless electrical stimulation and active ions, *Adv. Healthcare Mater.* 12 (17) (2023) e2300064, <https://doi.org/10.1002/adhm.202300064>.
- [14] F. Hashemi-Afzal, H. Fallahi, F. Bagheri, M.N. Collins, M.B. Eslaminejad, H. Seitz, Advances in hydrogel design for articular cartilage regeneration: a comprehensive review, *Bioact. Mater.* 43 (2024) 1–31, <https://doi.org/10.1016/j.bioactmat.2024.09.005>.
- [15] X. Li, S. Sheng, G. Li, et al., Research progress in hydrogels for cartilage organoids, *Adv. Healthcare Mater.* 13 (22) (2024) e2400431, <https://doi.org/10.1002/adhm.202400431>.
- [16] C. Shen, Z. Zhou, R. Li, et al., Silk fibroin-based hydrogels for cartilage organoids in osteoarthritis treatment, *Theranostics* 15 (2) (2025) 560–584, <https://doi.org/10.7150/thno.103491>.
- [17] Z. Chen, H. Zhang, J. Huang, et al., DNA-encoded dynamic hydrogels for 3D bioprinted cartilage organoids, *Mater. Today Bio.* 31 (2025) 101509, <https://doi.org/10.1016/j.mtbio.2025.101509>.
- [18] Z.X. Ma, Y. Wu, G.F. Li, J.L. Liu, Z. Geng, J.C. Su, Extracellular vesicles-loaded DNA hydrogels: a promising candidate for cartilage organoids engineering, *Chem. Eng. J.* 477 (2023) 147146, <https://doi.org/10.1016/j.cej.2023.147146>.
- [19] H. Zhang, S. Wu, W. Chen, Y. Hu, Z. Geng, J. Su, Bone/cartilage targeted hydrogel: strategies and applications, *Bioact. Mater.* 23 (2022) 156–169, <https://doi.org/10.1016/j.bioactmat.2022.10.028>.
- [20] H. Xie, G. Shi, R. Wang, et al., Bioinspired wet adhesive carboxymethyl cellulose-based hydrogel with rapid shape adaptability and antioxidant activity for diabetic wound repair, *Carbohydr. Polym.* 334 (2024) 122014, <https://doi.org/10.1016/j.carbpol.2024.122014>.
- [21] C.K. Balavigneswaran, V. Muthuvijayan, Nanohybrid-reinforced gelatin-ureidopyrimidinone-based self-healing injectable hydrogels for tissue engineering applications, *ACS Appl. Bio Mater.* 4 (6) (2021) 5362–5377, <https://doi.org/10.1021/acsabm.1c00458>.
- [22] I.M. El-Sherbiny, M.H. Yacoub, Hydrogel scaffolds for tissue engineering: progress and challenges, *Glob. Cardiol. Sci. Pract.* (3) (2013) 316–342, <https://doi.org/10.5339/gcsp.2013.38>, 2013.
- [23] Y. Chen, P. Ni, R. Xu R, et al., Tough and on-demand detachable wet tissue adhesive hydrogel made from catechol derivatives with a long aliphatic side chain, *Adv. Healthcare Mater.* 12 (29) (2023) e2301913, <https://doi.org/10.1002/adhm.202301913>.
- [24] H. Ren, Z. Zhang, X. Cheng, Z. Zou, X. Chen, C. He, Injectable, self-healing hydrogel adhesives with firm tissue adhesion and on-demand biodegradation for sutureless

- wound closure, *Sci. Adv.* 9 (33) (2023) eadh4327, <https://doi.org/10.1126/sciadv.adh4327>.
- [25] W. Zhao, X. Chen, Z. Han, et al., Nanoenzymes-integrated and microenvironment self-adaptive hydrogel for the healing of burn injury and post-burn depression, *Adv. Sci.* (2024) e2413032, <https://doi.org/10.1002/adv.202413032>.
- [26] X. Lin, Z. Huang, H. Huang, et al., A tough Janus poly(vinyl alcohol)-based hydrogel for wound closure and anti postoperative adhesion, *Acta Biomater.* 188 (2024) 103–116, <https://doi.org/10.1016/j.actbio.2024.08.049>.
- [27] X. Li, Z.L. Wang, W. Li, J.Q. Sun, Superstrong water-based supramolecular adhesives derived from poly(vinyl alcohol)/Poly(acrylic acid) complexes, *ACS Mater. Lett.* 3 (6) (2021) 875–882, <https://doi.org/10.1021/acsmaterialslett.1c00167>.
- [28] S. Barrientos, H. Brem, O. Stojadinovic, M. Tomic-Canic, Clinical application of growth factors and cytokines in wound healing, *Wound Repair Regen.* 22 (5) (2014) 569–578, <https://doi.org/10.1111/wrr.12205>.
- [29] C.R. Dumitrescu, I.A. Neacsu, R. Trusca, et al., Piezoelectric biocomposites for bone grafting in dentistry, *Polymers* 15 (11) (2023) 2446, <https://doi.org/10.3390/polym15112446>.
- [30] F. Acciarietti, S. Vesentini, L. Cipolla, Fabrication strategies towards hydrogels for biomedical application: chemical and mechanical insights, *Chem. Asian J.* 17 (22) (2022) e202200797, <https://doi.org/10.1002/asia.202200797>.
- [31] Q. Ding, S. Zhang, X. Liu, et al., Hydrogel tissue bioengineered scaffolds in bone repair: a review, *Molecules* 28 (20) (2023) 7039, <https://doi.org/10.3390/molecules28207039>.
- [32] M. Mohammadi, M. Karimi, B. Malaekhe-Nikouei, M. Torkashvand, M. Alibolandi, Hybrid in situ-forming injectable hydrogels for local cancer therapy, *Int. J. Pharm.* 616 (2022) 121534, <https://doi.org/10.1016/j.ijpharm.2022.121534>.
- [33] W.P. Chen, D.Z. Hao, W.J. Hao, X.L. Guo, L. Jiang, Hydrogel with ultrafast self-healing property both in air and underwater, *ACS Appl. Mater. Interfaces* 10 (1) (2018) 1258–1265, <https://doi.org/10.1021/acsami.7b17118>.
- [34] C. Fu, L. Shen, L. Liu, et al., Hydrogel with robust adhesion in various liquid environments by electrostatic-induced hydrophilic and hydrophobic polymer chains migration and rearrangement, *Adv. Mater.* 35 (15) (2023) e2211237, <https://doi.org/10.1002/adma.202211237>.
- [35] Z. Zhang, X. Li, Z. Peng, et al., Active self-assembly of piezoelectric biomolecular films via synergistic nanoconfinement and in-situ poling, *Nat. Commun.* 14 (1) (2023) 4094, <https://doi.org/10.1038/s41467-023-39692-y>.
- [36] F. Li, D. Lin, Z. Chen, et al., Ultrahigh piezoelectricity in ferroelectric ceramics by design, *Nat. Mater.* 17 (4) (2018) 349–354, <https://doi.org/10.1038/s41563-018-0034-4>.
- [37] B.Y. Lee, J. Zhang, C. Zueger, et al., Virus-based piezoelectric energy generation, *Nat. Nanotechnol.* 7 (6) (2012) 351–356, <https://doi.org/10.1038/nnano.2012.69>.
- [38] P. Chen, C. Xu, P. Wu, et al., Wirelessly powered electrical-stimulation based on biodegradable 3D piezoelectric scaffolds promotes the spinal cord injury repair, *ACS Nano* 16 (10) (2022) 16513–16528, <https://doi.org/10.1021/acsnano.2c05818>.
- [39] K.A. Fransen, S.H.M. Av-Ron, T.R. Buchanan, et al., High-throughput experimentation for discovery of biodegradable polyesters, *Proc. Natl. Acad. Sci. U. S. A.* 120 (23) (2023) e2220021120, <https://doi.org/10.1073/pnas.2220021120>.
- [40] J. Qiong, Z. Xia, L. Jing, W. Haibin, Synovial mesenchymal stem cells effectively alleviate osteoarthritis through promoting the proliferation and differentiation of meniscus chondrocytes, *Eur. Rev. Med. Pharmacol. Sci.* 24 (4) (2020) 1645–1655, <https://doi.org/10.26355/eurrev.202002.20338>.
- [41] K. Zheng, X. Zheng, M. Yu, Y. He, D. Wu, BMSCs-seeded interpenetrating network GelMA/SF composite hydrogel for articular cartilage repair, *J. Funct. Biomater.* 14 (1) (2023) 39, <https://doi.org/10.3390/jfb14010039>.
- [42] X. Zhang, L. Bai, J. Zhou, et al., Injectable microspheres adhering to the cartilage matrix promote rapid reconstruction of partial-thickness cartilage defects, *Acta Biomater.* 179 (2024) 220–233, <https://doi.org/10.1016/j.actbio.2024.03.021>.
- [43] X. Hu, M. Jin, K. Sun, et al., Type II collagen scaffolds repair critical-sized osteochondral defects under induced conditions of osteoarthritis in rat knee joints via inhibiting TGF- β -Smad1/5/8 signaling pathway, *Bioact. Mater.* 35 (2024) 416–428, <https://doi.org/10.1016/j.bioactmat.2024.02.008>.
- [44] N. van Gestel, S. Stegen, G. Eelen, et al., Lipid availability determines fate of skeletal progenitor cells via SOX9, *Nature* 579 (7797) (2020) 111–117, <https://doi.org/10.1038/s41586-020-2050-1>.
- [45] L. Ricotti, A. Cafarelli, C. Manferdini, et al., Ultrasound stimulation of piezoelectric nanocomposite hydrogels boosts chondrogenic differentiation *in vitro*, in both a normal and inflammatory milieu, *ACS Nano* 18 (3) (2024) 2047–2065, <https://doi.org/10.1021/acsnano.3c08738>.
- [46] Z. Han, F. Wang, W. Xiong, et al., Precise cell type electrical stimulation therapy via force-electric hydrogel microspheres for cartilage healing, *Adv. Mater.* (2024) e2414555, <https://doi.org/10.1002/adma.202414555>.
- [47] H. Zhang, D. Cai, X. Bai, Macrophages regulate the progression of osteoarthritis, *Osteoarthr. Cartil.* 28 (5) (2020) 555–561, <https://doi.org/10.1016/j.joca.2020.01.007>.
- [48] H. Sun, M. Zhan, Y. Zou, et al., Bioactive phosphorus dendrimers deliver protein/drug to tackle osteoarthritis via cooperative macrophage reprogramming, *Biomaterials* 316 (2025) 122999, <https://doi.org/10.1016/j.biomaterials.2024.122999>.
- [49] R.C. McDonough, C. Price, Targeted activation of G-protein coupled receptor-mediated Ca^{2+} signaling drives enhanced cartilage-like matrix formation, *Tissue Eng.* 28 (9–10) (2022) 405–419, <https://doi.org/10.1089/ten.TEA.2021.0078>.
- [50] G.Q. Xia, M.P. Zhu, J.W. Li, H. Huang, An alkaloid from Menispermum dauricum, dauricine mediates Ca^{2+} influx and inhibits NF- κ B pathway to protect chondrocytes from IL-1 β -induced inflammation and catabolism, *J. Ethnopharmacol.* 321 (2024) 117560, <https://doi.org/10.1016/j.jep.2023.117560>.
- [51] N. Alphonse, J.J. Wanford, A.A. Voak, et al., A family of conserved bacterial virulence factors dampens interferon responses by blocking calcium signaling, *Cell* 185 (13) (2022) 2354–2369, <https://doi.org/10.1016/j.cell.2022.04.028>, e17.
- [52] J. Yu, H. Liu, R. Gao, et al., Calcineurin: an essential regulator of sleep revealed by biochemical, chemical biological, and genetic approaches, *Cell Chem. Biol.* S2451–9456 (24) (2024), <https://doi.org/10.1016/j.chembiol.2024.12.003>, 00513–0.
- [53] X. Ren, H. Zhuang, B. Li, F. Jiang, Y. Zhang, P. Zhou, Gsmx4 alleviated osteoarthritis through piezo1/calcineurin/NFAT1 signaling Axis under excessive mechanical strain, *Int. J. Mol. Sci.* 24 (4) (2023) 4022, <https://doi.org/10.3390/ijms24044022>.
- [54] Y. Atsuta, R.R. Tomizawa, M. Levin, C.J. Tabin, L-type voltage-gated Ca^{2+} channel CaV1.2 regulates chondrogenesis during limb development, *Proc. Natl. Acad. Sci. U. S. A.* 116 (43) (2019) 21592–21601, <https://doi.org/10.1073/pnas.1908981116>.
- [55] M. Tomita, M.I. Reinhold, J.D. Molkenin, M.C. Naski, Calcineurin and NFAT4 induce chondrogenesis, *J. Biol. Chem.* 277 (44) (2002) 42214–42218, <https://doi.org/10.1074/jbc.C200504200>.
- [56] J. Abramson, J. Adler, J. Dunger, et al., Accurate structure prediction of biomolecular interactions with AlphaFold 3, *Nature* 630 (8016) (2024) 493–500, <https://doi.org/10.1038/s41586-024-07487-w>.
- [57] M. Yao, G.W. Miller, B.N. Vardarajan, A.A. Baccarelli, Z. Guo, Z. Liu, Deciphering proteins in Alzheimer's disease: a new Mendelian randomization method integrated with AlphaFold3 for 3D structure prediction, *Cell Genom* 4 (12) (2024) 100700, <https://doi.org/10.1016/j.xgen.2024.100700>.
- [58] T.B. Dunlap, E.C. Cook, J. Rumi-Masante, H.G. Arvin, T.E. Lester, T.P. Creamer, The distal helix in the regulatory domain of calcineurin is important for domain stability and enzyme function, *Biochemistry* 52 (48) (2013) 8643–8651, <https://doi.org/10.1021/bi400483a>.
- [59] B. Sun, D. Vaughan, S. Tikunova, T.P. Creamer, J.P. Davis, P.M. Kekenus-Huskey, Calmodulin-calcineurin interaction beyond the calmodulin-binding region contributes to calcineurin activation, *Biochemistry* 58 (39) (2019) 4070–4085, <https://doi.org/10.1021/acs.biochem.9b00626>.
- [60] J.P. Northrop, S.N. Ho, L. Chen, et al., NF-AT components define a family of transcription factors targeted in T-cell activation, *Nature* 369 (6480) (1994) 497–502, <https://doi.org/10.1038/369497a0>.
- [61] C. Nusbaum, M.C. Zody, M.L. Borowsky, et al., DNA sequence and analysis of human chromosome 18, *Nature* 437 (7058) (2005) 551–555, <https://doi.org/10.1038/nature03983>.

Abbreviations

AA: acrylic acid
 ACAN: Aggrecan
 AF3: AlphaFold3
 ANOVA: analysis of variance
 BIS: N,N'-methylenebisacrylamide
 BMSCs: bone marrow mesenchymal stem cells
 CaM: calmodulin
 CaN: calcineurin
 CCB: calcium channel blockers
 CCK-8: cell counting kit-8
 COL2A1: COL II alpha 1 chain
 CS: chitosan
 DIO: 3,3'-diocetadecyloxacarbocyanine perchlorate
 ES: electrostimulation
 FTIR: fourier transform infrared
 GAGs: glycosaminoglycans
 Hyd-KNN: PVA/PAA/CS/KNN hydrogel
 Hyd: PVA/PAA/CS hydrogel
 H&E: hematoxylin-eosin
 KNN: sodium potassium niobate
 Hyd-6: 6 wt% KNN Hyd-KNN
 ICRS: international cartilage repair society
 IHC: immunohistochemistry
 IL-6: interleukin 6
 KPS: potassium persulfate
 MAPK: mitogen-activated protein kinases
 MMP-13: matrix metalloproteinase 13
 MRI: magnetic resonance imaging
 NFATc1: nuclear factor of activated T-cells cytoplasmic 1
 PAA: polyacrylic acid
 PBS: phosphate buffer saline
 PET: polyethylene terephthalate
 PFM: piezoresponse force microscope
 PT: piezocatalytic therapy
 PVA: polyvinyl alcohol
 SEM: scanning electron microscopy
 SMSCs: synovial mesenchymal stem cells
 SOX9: SRY-Box transcription factor 9
 TEM: transmission electron microscopy
 TEMED: tetramethylethylenediamine
 US: ultrasound

VGCC: voltage-gated calcium channels

XRD: X-ray diffractometer